DESIGN OF HIGH Q THIN FILM BULK ACOUSTIC WAVE RESONATOR FOR FILTER APPLICATIONS

By

Thi Bich Ngoc Nguyen

Submitted to the Faculty of Technology and Maritime Science

in Partial Fulfillment of the Requirements for the Degree of

Master of Science in Micro and Nano Systems Technology

at

Buskerud and Vestfold University College

Supervisors: **Prof. Ulrik Hanke**
Assoc. Prof. Agne Johannessen

May 2014

To my parents and sister

Abstract

The inevitable propagation of Lamb waves in a traditional Thin Film Bulk Acoustic Wave Resonator (FBAR) leads to the lateral leakage of energy from the active region of the device, and consequently corresponds to a degradation of its quality factors (Q factors). The use of a frame on the periphery of an FBAR is reported to improve the Q factors potentially providing better filter performance for demanding mobile/wireless communication applications. This frame performs as a Bragg reflector which is able to prevent the Lamb waves from leaking to the outside by forcing them to reflect back into the active region of the resonator. A single frame that can reflect one particular Lamb mode has been introduced in literature. This work focuses on a more advanced frame structure for the FBAR. It introduces the procedure to design a dual frame with the ability to reflect the two Lamb modes that presumably contribute most to acoustic leakage – the zero and the first order symmetric mode (S_0 and S_1).

The displacement field of a W/AlN/W stack FBAR is found from 2D Finite Element Simulations (FEM). Then the dispersion diagrams for the Lamb modes in the active as well as the frame regions are extracted from taking the Fourier transform of the displacement field of the layer stack. From this the lateral propagation constants for the S_0 and S_1 modes at anti–resonance frequency (f_a) are obtained for the various regions. Adopting the diffraction grating method from optics, a single frame designed for dual–mode reflection at f_a can be achieved if the width of the frame is multiples of the quarter wavelengths of both modes. The mentioned dual frame is the combination of these two single frames with different step heights.

FEM simulation results for various frame configurations of the FBAR, including the basic FBAR structure without a frame, the one with a single frame that can only reflect S_1 mode, and the ones designed for the dual–mode reflection, involving a single frame and an advanced dual frame are extracted from COMSOL software. These simulations are carried out in order to compare the effectiveness of different frame designs. Among all, the FBAR with a dual frame provides the highest Q factors. In addition, the ripples located at the frequencies near and above f_a are suppressed, giving a smoother electrical characteristic of the resonator at these frequencies.

Acknowledgements

I would like to express my sincere gratitude to my supervisors Prof. Ulrik Hanke and Assoc. Prof. Agne Johannessen for what they have done for me, both academic and non–academic things. They have shown me the right way and given me precious advices and related literature during my thesis work with their patience, enthusiasm and deep knowledge.

I am thankful to Prof. Lars Hoff, Prof. Einar Halvorsen, Prof. Kaiying Wang as well as Cuong Phu Le, Tung Manh, Zekija Ramic, Thi Thuy Luu, Anh Tuan Thai Nguyen for spending time answering my academic questions.

I also want to convey my thanks to my fellow master students in HBV for all of their support towards my work.

Last but not least, I thank my family and close friends for giving me the encouragement on finishing this thesis.

Help is always given to me whenever I ask for. I am truly grateful for everything.

Summer 2014,

Contents

List of Figures

List of Tables

CHAPTER 1. Introduction

1.1 FBAR – History and Applications in Wireless Telecommunication

Thin Film Bulk Acoustic Wave Resonator (FBAR) was first introduced by K. M. Lakin and J. S. Wang in the early 1980 [1] as a method to apply Bulk Acoustic Wave (BAW) theory in real devices. BAW resonators are piezoelectric acoustic devices in which the acoustic waves are generated and propagate in the vertical direction of the structure. Due to these waves, the devices vibrate at a resonance frequency related to the thickness of the piezoelectric layer and the electrodes as well as other layers, e.g. supporting layers. BAW resonators are categorized into FBAR and Solidly Mounted Resonators (SMR) which physical principles, in general, are the same. The only difference is the fabrication technology to provide the acoustical confinement to obtain a high quality factor. SMR implements a set of alternating low and high acoustic impedance stacks, known as Bragg reflector or Bragg mirror, to reflect the acoustic waves back to the piezoelectric layer while in FBAR, an air–gap cavity is created below the bottom electrode, taking advantage of the large acoustic impedance mismatch between the electrode and air to confine the waves to the piezo–layer (Figure 1.1). The fact that the resonance frequency of BAW ranges from 1 GHz to 10 GHz and even higher [2] makes it meet the demand for various radio frequency (RF) systems, e.g. mobile telecommunication, satellite communication and other wireless devices. One of the well–known applications of BAW in such systems is the filter. The idea is that a bandpass RF filter for rejecting unwanted frequencies can be achieved by utilizing various filter configurations, i.e. the arrangement of more–than–two BAW resonators, such as ladder, stacks, balanced bridge, lattice topology. Two RF filters, one for the transmitter (Tx) and another for the receiver (Rx) with a certain separation between their respective bands, construct the duplexer in a cell phone.

Why BAW filters? Traditional ceramic filter and matured Surface Acoustic Wave (SAW) filter technology has been used over years for RF filter purposes. However, ceramic filters tend to come in large physical size hence are not much ideal for modern circuit integration. SAW provides small size devices with high performance, tolerable insertion loss and good rejection up to 1.5 GHz [3, 4]. Being first explained in 1885 by Lord Rayleigh, SAWs have been developed and applied in mobile telephony for about 20 years [5] and are widely used in 2G receiver filters and duplexers. Then 3G with application frequency range of 1.8 –

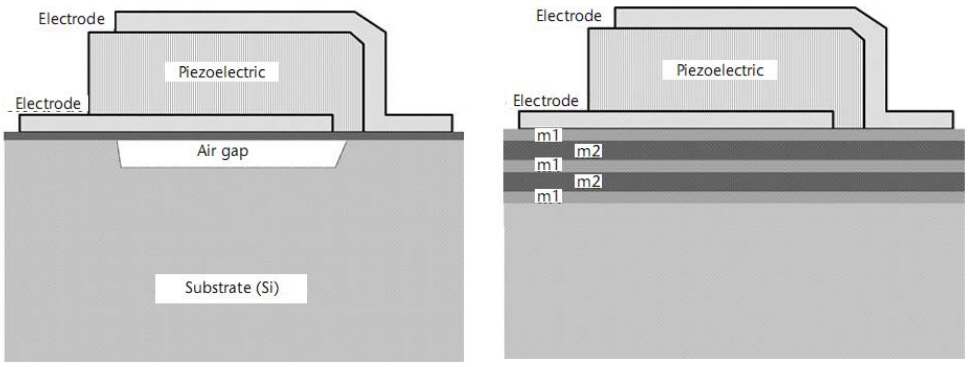

(a) (b)

Figure 1.1. 2D schematic of FBAR (a) and SMR (b) [6]

2.5 GHz and 4G/LTE with the range of 2.0 – 8.0 GHz came into the picture, entailing the higher complexity of the system and demand of filter performance. For frequencies beyond 2 GHz, SAW filters no longer fulfill the requirements of insertion loss, pass-band skirt steepness and power handling control. In addition to the degradation of electrical performance, SAW filters also reveal the decline of selectivity and the high sensitivity to temperature variations. It is BAW (both FBAR and SMR) that could complement SAW filter in such frequency range with low loss, better performance, less sensitive to temperature changes, higher power capability and good compatibility with standard IC technology. The thickness of BAW even decreases with the frequency, especially in FBAR, and agrees with high level integrated circuits [2]. BAW is therefore well suited for 3G and 4G mobile telecommunication technology as well as other wireless applications which operating frequencies fall above 2 GHz.

Due to such convincing performance advantages at super high frequency range over SAW, the world has witnessed the evolution of BAW devices in the industry since TFR Technologies and Lakin developed the first FBAR product in 1989, then followed by Agilent and Ruby in 1994 [7]. Afterwards, many companies joined the market and reported their BAW products for various filter bands. Infineon Technologies AG, in 2002, produced SMR devices in volume; subsequently came TriQuint Semiconductor, with the same technology for mobile handset and 3G/4G cellular base station applications at 1.9 and 2.4 GHz. In the early of 2013, TriQuint released 3 new BAW RF filters for Band 2: 1.93 – 1.99 GHz and 1.85 – 1.91 GHz, and Band 7: 2.50 – 2.57 GHz passband; Skyworks introduced industry's first BAW filters to enable WiMAX and WLAN co–existence in 2008 with two products, SKY33107 and SKY33108 which, according to them, exhibit excellent rejection – in the 2.4 GHz WLAN band for the former, and 2.495 – 2.690 GHz WiMAX band for the latter one; In 2008, AVAGO

Technologies acquired Infineon's BAW business and became the leading filter and duplexer manufacturer for wireless applications. Their FBAR filtering technology has supported as many as 15 different frequency bands for 4G/LTE requisitions in recent years.

1.2 Motivation and Purpose of the Thesis

Despite of the maturity over more than 30 years of historical research and development, there is still space for those that work on optimization of the state–of–the–art FBAR in both performance and manufacturing technology aspects. The evolution of smartphones with their ongoing generation of network, e.g. 3G, 4G/LTE and other wireless access methods, e.g. WiFi, Bluetooth, GPS receiver path have increased the need for advanced filter technology. The filters are required to be extremely high selectivity to ensure that the signals from close RF bands do not interfere with each others. The bandpass RF filters therefore must have very steep skirts, or in terms of physics and engineering, very high Q factors of the element resonators. Being a branch of BAW resonator family, FBAR provides even better Q factors than its brother technology – SMR (while SMR reveals better mechanical handling as a trade–off). However, due to recent demanding, the FBAR design is still needed to be optimized for superior Q factors, and thus, filter performance. The operation of FBAR is based on the through–thickness longitudinal acoustic waves, so the waves propagating in lateral direction are undesirable and may lead to two consequences. Firstly, they leak to outside region of the resonator. Secondly, they generate unwanted satellite resonances near the main resonance, resulting in the so–called spurious modes. It is not only the acoustic leakage but also the lateral spurious modes that steal energy from the main mode and take responsibility for the degradation of Q factors of the resonator [8]. At least three methods have been proposed to solve the arising problems [9]: (a) flattening the resonator's TE1 dispersion curve, (b) apodization, (c) lateral edge design, or frame method. The first two methods [10-13] in fact do not eliminate the spurious modes. They smear and smooth out the peaks of the satellite resonances by creating larger number of weak spurious modes instead of small number of strong ones, hence minimize the effects of these modes on the electrical characteristic. However, the Q value is not significantly improved since the amount of energy stolen by the unwanted modes remains the same. In addition, these two methods do not solve the leakage problem. The third one, on the other hand, promises significant effectiveness on increasing the Q factors. In this method, a frame is constructed in the border region of the FBAR by adding more material to that region. There

are two techniques for designing this frame. The first one focuses on inhibiting the leakage of acoustic waves. The second one is to modify the lateral boundary condition so that only the fundamental mode (or piston mode) can couple with the driving field. By this way, the spurious modes can be suppressed. Many works have focused on the later direction since 2003 when J. Kaitila et. al. published an article about a spurious free resonator (SMR) using such frame method. They proved that the spurious modes in the traditional resonator are eliminated with precisely designed border region [14]. A patent of this concept for FBAR was filed in 2004 and granted to Feng et. al. in 2007 [15]. Also in the year of 2004, R. Thalhammer et. al., based on electrical measurements and laser interferometry, confirmed the theoretical prediction about the improvement of such resonator's performance [16]. A publication of G. Fattinger in 2005 [17] explained the physics behind the frame in an SMR using the dispersion scheme. In 2006, R. Thalhammer et. al. designed a AlN–based FBAR resonator in which combined a recessed and a raised frame [18]. By varying the depth of the etched as well as the overlapped region to a correct amount, they demonstrated the elimination of the spurious modes in the resonator response. The efficiency of the frame concept was once again affirmed by T. Pensala in 2009 [19] when he investigated an optimized ZnO–based SMR by both modeling and experiment. In 2012, M. Hara applied numerical method [20] and finite element method (FEM) [21] to show the suppression of spurious modes in a frame–added AlN–based FBAR operating at 2.5 GHz. In a recent article published in 2013 [22], P. Kumar and A. Tripathi simulated a design of a new step–like frame FBAR which border region comprises three raised frames instead of one as in previous research. Their designed FBAR resonates at 1.5 GHz and the unwanted resonances are effectively removed.

It can be seen that since the first proposal by Kaitila, research mainly focused on generating the piston mode to get rid of the spurious modes in order to improve the Q factors. In addition, the design rules for such frame have not yet been disclosed and the leakage problem was somewhat underestimated. This thesis, instead of following the mentioned works, uses the same frame method to enhance the Q factors in a completely different manner – by focusing on preventing the lateral wave leakage. A design rule for the frame is also proposed. In Chapter 5 of [23], written by R. Ruby, it is argued that the raised frame belongs to part of a lateral Bragg reflector that inhibits energy loss due to leakage. To clarify the argument, in this thesis, a full lateral acoustic Bragg mirror will be placed onto the edge of the top electrode of an AlN–based FBAR to

efficiently reflect the escaping waves and trap them inside the resonator active region.

A traditional vertical Bragg reflector obeying the quarter–wavelength rule can only reflect the longitudinal waves. Therefore, in order to make an advanced dual–wave reflector in which both the longitudinal and shear waves are optimally reflected, S. Jose presented a new design procedure for the acoustic mirror [24, 25]. In this thesis, the design rule of the Bragg mirror that Jose recommended for an SMR in vertical direction is now utilized in the lateral dimension of an FBAR for reflecting two strongest coupled lateral waves, aiming for a prior target – the enhancement of Q values.

A 2D model of FBAR is built and simulated in COMSOL multiphysics software for design and analysis purposes. In the simulation, the material and thickness of the layers will be taken into account in order to obtain an acceptable k_{eff}^2 at a certain operating frequency.

In addition to the optimization work, this thesis also provides deep insight about FBAR structure and the formation of lateral waves, known as Lamb waves, as well as the loss mechanisms caused by them, based mainly on acoustic wave theory and the dispersion concept.

CHAPTER 2. Basics of FBAR

2.1 The Concept of FBAR

A simple FBAR comprises a thin piezoelectric–material film sandwiched between two metal electrodes called top and bottom electrode, as shown in Figure 2.1. The metalized area where these two electrodes overlap is the active region. Elsewhere it is called the outside region, or the "swimming pool" in some literature [15, 23, 26]. Under the bottom electrode, an air–gap cavity is created to make use of the exceedingly high difference in acoustic impedance between the electrode material and air – a strategy for acoustic energy trapping. This air–gap cavity isolates the active area from any mechanical contact beneath it, resulting in the so– called "Thin Film" name and distinguishing FBAR from SMR which implements acoustic Bragg reflector for the same purpose.

Being a category of BAW resonators, FBAR operates based on the propagation of the acoustic waves inside its body in thickness direction, i.e. between the top and bottom electrode. The acoustic wave in nature is the commotions of the particles that propagate in an elastic medium, entailing the mechanical deformation of the medium along the propagation axis or any other axes. Unlike electromagnetic waves, acoustic waves require a material medium in order to transfer their energy, supplied by an excitation source, from one location to another in the form of particle disturbances. The high operating frequency of FBAR, therefore, does not come from its structural natural vibration, which is only in kHz range. Instead, the excitement of the acoustic waves inside an FBAR makes it resonate at acoustic frequency, falling within GHz range. This frequency is in orders higher than the other one hence will not be affected by the structural vibration.

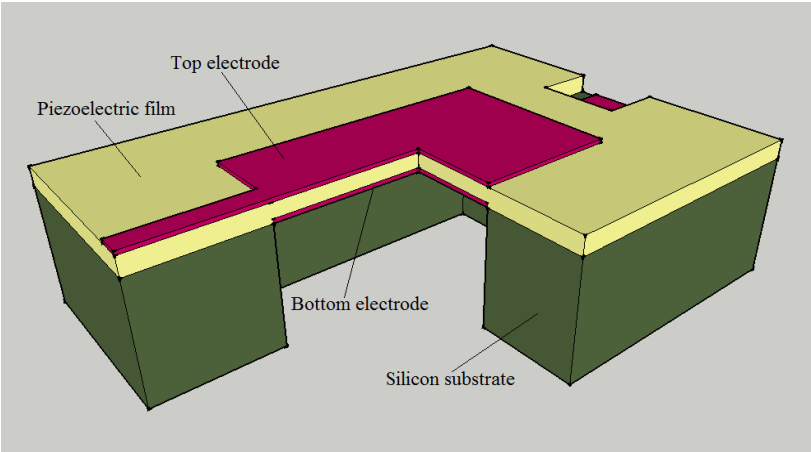

Figure 2.1. Illustration of the FBAR

The excitation source of FBAR is an alternating voltage applied to the electrodes of the resonator. The electromagnetic energy from this electrical source is transformed into the acoustic energy via a mechanism termed "piezoelectric" phenomenon, which will be further studied in section 2.2.

2.2 Acoustic Waves in Piezoelectric Material

2.2.1 Propagation of Acoustic Waves

For a non–piezoelectric thin film that has an acoustic velocity of v_a, also known as wave velocity, and a thickness of d, then the pure mechanical resonance of the resonator is achieved whenever d is equal to an integer multiple of half of a wavelength of the acoustic wave

$$d = (n+1)\frac{\lambda}{2} = (n+1)\frac{v_a}{2f_n} \qquad n = 0,1,2,... \tag{2.1}$$

where f_n is the thickness–dependent resonance frequency of a BAW resonator operating in longitudinal mode

$$f_n = (n+1)\frac{v_a}{2d} \tag{2.2}$$

The resonator, in this circumstance, is called a half–wavelength resonator and the mode corresponding to $n = 0$ is the fundamental longitudinal mode. A mode is a solution to the wave equation and represents for a certain type of travelling wave. In the bulk, acoustic waves can propagate in three modes – longitudinal mode, shear mode and the combination of both [6]. In longitudinal mode, the vibration of the particles is along the wave propagation direction, leading to the local compression and elongation of the material in that direction. For this reason, the longitudinal mode is also defined as the thickness–extensional wave, or TE mode and is depicted in Figure 2.1a. The fundamental longitudinal mode is the main operating mode of an FBAR. On the other hand, in shear mode, the particle motion is perpendicular to wave propagation direction with no variation in local mass density [23] as shown in Figure 2.2b.

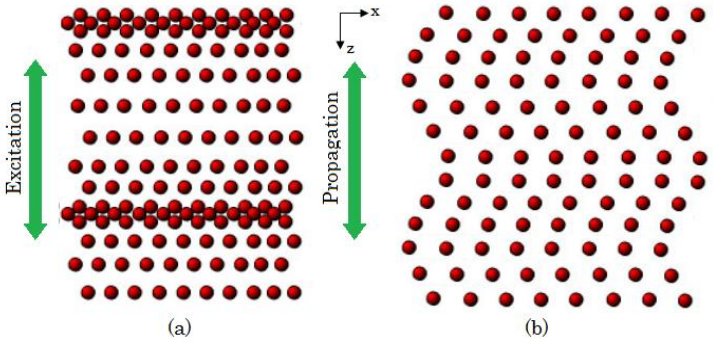

Figure 2.2. Longitudinal (a) and shear wave (b) in thickness dimension

The FBAR is considered to be the waveguide of the fundamental mode along z–axis. The guided mode is thus assumed to be proportional to $e^{-jk_z z}$ where k_z is called the propagation constant of the mode in z direction.

In advance to study about the piezoelectric effect in FBAR, the acoustic equation of motion is derived in order to provide the basic understandings about acoustic waves in any elastic materials. The derivation follows the analysis provided in [23] and [27]. As particles vibrate, due to the variation in crystalline structure of the material, internal force – called stress, and deformation – called strain are generated inside an elastic body. Define that T is stress, S is strain, u is vertical displacement and v is particle velocity, the net force over an infinitesimal area dA can be written in term of vertical stress component

$$dF = \frac{\partial T}{\partial z} dz dA \tag{2.3}$$

According to Newton's second law

$$F = ma \tag{2.4}$$

Hence

$$\frac{\partial T}{\partial z} dz dA = \rho dA \Delta z \frac{\partial^2 u}{\partial^2 t} \Rightarrow \frac{\partial T}{\partial z} = \rho \frac{\partial^2 u}{\partial^2 t} \tag{2.5}$$

Where m is the mass, ρ is the density and a is the acceleration corresponding to the second order of time derivative.

Particle velocity is expressed by the time derivative of particle displacement

$$v = \frac{\partial u}{\partial t} \tag{2.6}$$

While the stress in vertical direction is defined as the gradient of particle displacement with respect to position

$$S = \frac{\partial u}{\partial z} \tag{2.7}$$

Linear relation between stress and strain is given by Hooke's law with the introducing of stiffness constant c

$$T = cS \tag{2.8}$$

Combine three equations (2.6), (2.7) and (2.8), the time derivative of strain can be written as

$$\begin{cases} \dfrac{\partial S}{\partial t} = \dfrac{\partial^2 u}{\partial z \partial t} = \dfrac{\partial v}{\partial z} \\ \dfrac{\partial S}{\partial t} = \dfrac{1}{c} \dfrac{\partial T}{\partial t} \end{cases} \Rightarrow \quad \frac{\partial^2 v}{\partial z \partial t} = \frac{1}{c} \frac{\partial^2 T}{\partial^2 t} \tag{2.9}$$

By differentiating (2.5) with respect to z, the following relation can be achived

$$\frac{1}{\rho}\frac{\partial^2 T}{\partial^2 z} = \frac{\partial^3 u}{\partial^2 t \partial z} = \frac{\partial^2 v}{\partial z \partial t} \tag{2.10}$$

From (2.9) and (2.10) the well–known one dimensional wave equation can be obtained

$$\frac{1}{\rho}\frac{\partial^2 T}{\partial^2 z} = \frac{1}{c}\frac{\partial^2 T}{\partial^2 t} \quad \Rightarrow \quad \frac{c^2}{\rho}\frac{\partial^2 S}{\partial^2 z} = \frac{c^2}{c}\frac{\partial^2 S}{\partial^2 t}$$

$$\Rightarrow \quad \frac{c}{\rho}\frac{\partial^2 u}{\partial^2 z} = \frac{\partial^2 u}{\partial^2 t} \tag{2.11}$$

The phase velocity v_a of acoustic waves is defined as in (2.12)[1] and should not be confused with the particle velocity v

$$v_a = \lambda * f = \sqrt{\frac{c}{\rho}} \tag{2.12}$$

And the acoustic impedance, which is a frequency dependent quantity, is

$$Z_a = \sqrt{\rho c} = \rho v_a \tag{2.13}$$

When any bulk wave arrives at the interface between two different materials with different acoustic impedance, it will be partly reflected and partly transmitted. The higher acoustic impedance difference, the better wave reflection is. Bulk waves are hence confined within top and bottom electrode, providing a powerful energy trapping scheme. This principle is effectively applied in FBAR with the presence of an air cavity under bottom electrode, making use of the very large acoustic impedance of electrode metal and the small one of air. Same strategy is also implemented in SMR by utilizing alternative high and low acoustic impedance layers to improve the reflectivity of the waves at each interface. However, as this kind of structure is not loss free, the Q value of an SMR tends to be lower than that of an FBAR in same band of frequency due to the vertical acoustic leakage through the Bragg reflector [4, 28]

2.2.2 The Piezoelectric Effect

Piezoelectricity is a phenomenon that exhibits the coupling between mechanical properties such as stress and strain and the electrical properties such as electric field strength E and electric displacement field D. The relationship of these two domains (mechanic and electric) is established via the polarization vector [27]. An applied electric field creates a polarization vector based on the separation of positive and negative charges in the crystal, called the dipole moment. The piezoelectric effect occurs when there is a coupling between

[1] λ is the wavelength of the fundamental longitudinal wave.

this polarization vector and the stress. Only the materials with special symmetry class of crystal structure can support this effect. They are addressed as the piezoelectric materials and are chosen as the FBAR acoustic layer for one essential reason: they improve the electromechanical energy conversion, thus promote the propagation of acoustic waves inside the layer.

Under an electrical excitation, FBAR generates mechanical resonances by converting electromagnetic waves to acoustic waves via its piezoelectric thin film. The power of the piezoelectric layer lies in its ability to relate mechanical displacement with the electrical quantities since piezoelectric materials become deformed when an electrical field is applied. For a pure electrical behavior, the linear relationship between D and E for a medium with no piezoelectric effect is denoted by

$$D = \varepsilon E \tag{2.14}$$

where the permittivity ε is a scalar. The relation in a pure mechanical event is expressed in (2.8). But once piezoelectricity is introduced in the medium, the presence of both electrical and mechanical quantities leads to the piezoelectric constitutive relations

$$T = c^E S - eE \tag{2.15}$$

$$D = eS + \varepsilon^S E \tag{2.16}$$

Three terms e, c^E, ε^S are all material parameters where e is the piezoelectric stress constant, c^E denotes the stiffness in a constant electric field and ε^S is the permittivity under constant strain. For anisotropic materials which parameters vary upon their crystallographic orientations, these constants are written in tensor with two–subscript–index elements. The first index refers to the axis of excitation and the second refers to that of actuation. For instance, in the fundamental mode of FBAR, the electric field is applied in z–axis coinciding with c–axis crystal orientation (the deformation direction), therefore the constants are denoted as e_{33}, c_{33}, ε_{33}.

Equations (2.15) and (2.16) expresses the electrical–mechanical and mechanical–electrical coupling in a piezoelectric film and can be rewritten as

$$T = c^E\left(1+\frac{e^2}{c^E\varepsilon^S}\right)S - \frac{e}{\varepsilon^S}D = \left(c^E+\frac{e^2}{\varepsilon^S}\right)S - \frac{e}{\varepsilon^S}D = c^D S - \frac{e}{\varepsilon^S}D \tag{2.17}$$

The fact $c^D > c^E$ implies that under the effect of piezoelectricity, actual acoustic velocity is higher than the one that is directly calculated from the material stiffness c^E. c^D is called the piezo–electrically stiffened elastic constant.

Based on the assumption that the lateral dimensions of the FBAR is infinitely wide and the electrodes are infinitely thin, the one–dimensional general ansatz for wave equation (2.11) can be written

$$u(z,t) = \left[a\sin(k_z z) + b\cos)(k_z z)\right]e^{j\omega t} \tag{2.18}$$

The term $e^{j\omega t}$ will be omitted in the following equations for presentation simplicity. Substitute (2.18) into (2.17)

$$T(z) = c^D S - \frac{e}{\varepsilon^S} D = c^D k\left[a\cos(k_z z) - b\sin(k_z z)\right] - \frac{e}{\varepsilon^S} D \tag{2.19}$$

Applying boundary condition $T(z = -d/2) = T(z = d/2) = 0$, gives

$$T(z) = c^D S - \frac{e}{\varepsilon^S} D = \frac{eD}{\varepsilon^S} \cdot \frac{\cos(k_z z)}{\cos(k_z d/2)} - \frac{eD}{\varepsilon^S} \tag{2.20}$$

The strain is now given by

$$S(z) = \frac{eD}{c^D \varepsilon^S} \frac{\cos(k_z z)}{\cos(k_z d/2)} \tag{2.21}$$

$$u(z) = \int S(z)dz = \frac{eD}{c^D \varepsilon^S k_z} \cdot \frac{\sin(k_z z)}{\cos(k_z d/2)} \tag{2.22}$$

From (2.16) and (2.17)

$$E = -\frac{e}{c^D \varepsilon^S} T + \left(\frac{1}{\varepsilon^S} - \frac{e^2}{c^D \varepsilon^{S2}}\right) D \tag{2.23}$$

The voltage applied to the body is

$$V = \int_{-d/2}^{d/2} E(z)dz = \frac{dD}{\varepsilon^S}\left[1 - \frac{e^2}{c^D \varepsilon^S} \frac{\tan(k_z d/2)}{k_z d/2}\right] \tag{2.24}$$

Assume that A is the active area of the FBAR, then the current at the electrodes is $I = j\omega AD$, and the impedance takes the form

$$Z = \frac{V}{I} = \frac{1}{j\omega C_0}\left[1 - k_t^2 \frac{\tan(k_z d/2)}{k_z d/2}\right] \tag{2.25}$$

The electromechanical coupling factor for vertical longitudinal wave is introduced as

$$k_t^2 = \frac{e^2}{c^D \varepsilon^S} \tag{2.26}$$

and the static capacitance of the parallel plate capacitor with piezoelectric material as its dielectric is

$$C_0 = \frac{\varepsilon^S A}{d} \tag{2.27}$$

where d is the thickness of the piezo–layer and A is the overlapping area of two metal electrodes.

2.3 Electrical Modeling and Characterization

2.3.1 Electrical Impedance Curve

The input electrical impedance of an FBAR is the line graph of Z in (2.25), including the amplitude and phase graphs, shown in Figure 2.3. They illustrate the main resonance characterized by two frequencies – f_r and f_a. The former stands for series resonance frequency, occurring when the amplitude of Z tends to zero and the later stands for anti–resonance frequency, occurring as the amplitude tends to infinity. Together, they form the so–called frequency pair of a resonator.

When $Z \to \infty$, it can be deduced from (2.25) that

$$\tan(k_z d/2) \to \infty \implies \frac{k_z d}{2} = (2n+1)\frac{\pi}{2} \qquad n = 0,1,2,\ldots$$

$$\Rightarrow \frac{2\pi f_{a,n} d}{2v_a} = (2n+1)\frac{\pi}{2} \Rightarrow f_{a,n} = (2n+1)\frac{v_a}{2d} \tag{2.28}$$

The difference between (2.2) and (2.28) indicates that under piezoelectric effect, the resonances do not include anti–symmetric modes of displacement, unlike in the case of pure mechanical resonances. Such modes cannot couple with a constant driving field and are therefore not excited [23]. The corresponding thickness of the FBAR for such condition of resonance is shown in Figure 2.4.

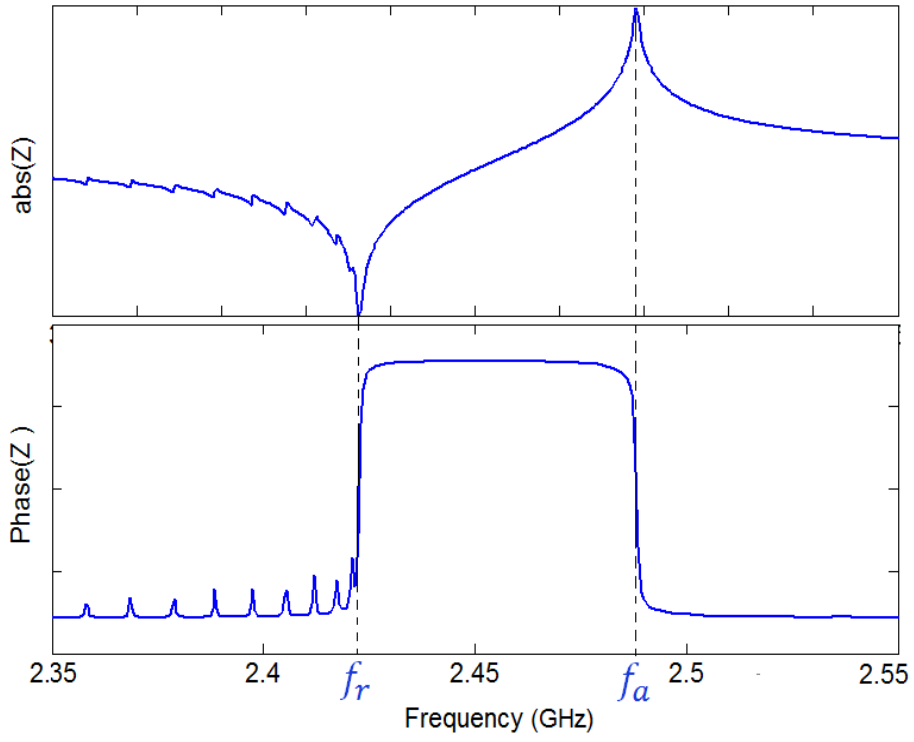

Figure 2.3. Amplitude (top graph) and phase plot (bottom graph) of electrical impedance Z of a simulated FBAR

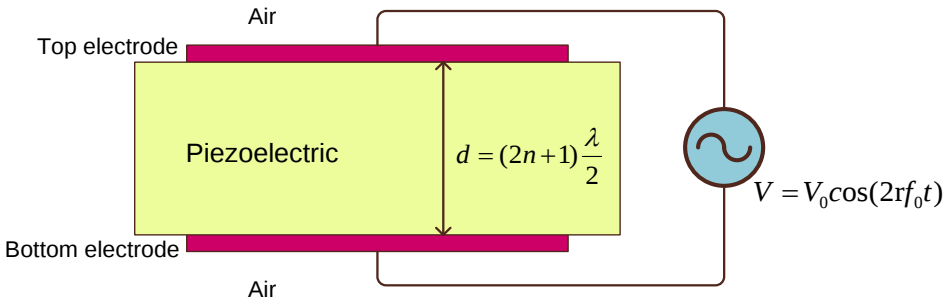

Figure 2.4. Schematic of an FBAR and its resonance condition

As $Z \to 0$, $f_{r,n}$ can be obtain from the equation

$$k_t^2 \frac{\tan(k_z d/2)}{k_z d/2} = 1 \implies k_t^2 = \frac{\pi}{2}\frac{f_r}{f_a}\cot\left(\frac{\pi}{2}\frac{f_r}{f_a}\right) \tag{2.29}$$

2.3.2 The Modified Butterworth Van Dyke (mBVD) Model

The mBVD model is an equivalent electrical circuit with lumped elements used to characterize an FBAR. This model shows its best role in practical measurement where electrical characteristics are obtained from a collection of measured data. This can be done by fitting the measured values into an mBVD circuit. The circuit is depicted in Figure 2.5 where C_0 is the static capacitance found in (2.27); R_0 corresponds to the dielectric losses of the associated material, loss due to spurious resonances and lateral wave leakage; R_m is the resistance associating with the mechanical losses of acoustic waves; L_m and C_m are motional inductance and capacitance related to process–dependent parameters and material properties [6]; serial resistance R_s is the associated resistance of the metal electrodes. The electrical input impedance takes the form

$$Z(\omega) = R_s + \frac{(R_0 + 1/j\omega C_0)(R_m + j\omega L_m + 1/j\omega C_m)}{R_0 + R_m + j\omega L_m + 1/j\omega C_0 + 1/j\omega C_m} = R(\omega) + jX(\omega) \tag{2.30}$$

where the resonance and anti–resonance frequency can be derived by requiring zero and infinite impedance amplitude. Approximately calculated, they are

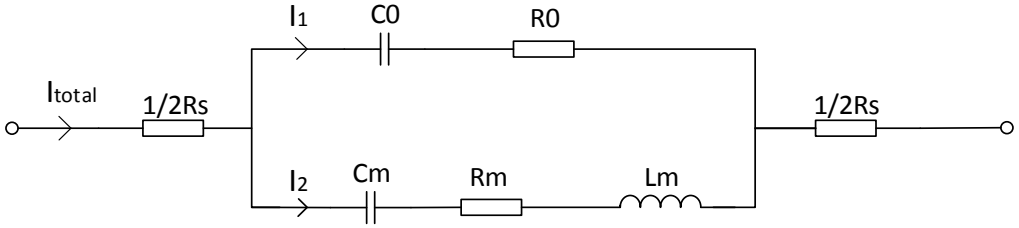

Figure 2.5. Modified Butterworth van Dyke model

$$\omega_r \approx \frac{1}{\sqrt{L_m C_m}} \quad \text{and} \quad \omega_a \approx \omega_r \sqrt{\frac{C_a + C_0}{C_0}} \tag{2.31}$$

2.3.3 The Smith Chart

The Smith chart was invented in 1929 by Philip H. Smith [29] as an powerful graphic tool to represent the complex reflection coefficient Γ and the terminating impedance. The Smith chart is actually a conformal mapping of complex $Z-$ plane onto $\Gamma-$ plane via the transformation

$$\Gamma = \frac{Z - Z_0}{Z + Z_0} = \frac{Z / Z_0 - 1}{Z / Z_0 + 1} = \frac{z - 1}{z + 1} \tag{2.32}$$

where Z_0 is the characteristic impedance of a transmission line, normally taking the value of 50Ω, and z is the normalized impedance. Figure 2.6 has shown the transformation by matching the colors in the left hand side image to those in the right one.

The upper semicircular of the chart is inductive since it corresponds to the positive imaginary part of Z whereas the lower one is capacitive as it expresses the negative imaginary part of Z. There are two important points in the chart, shown in Figure 2.7, that are worth investigating. The first one occurs when $\Gamma = -1$, or $z = 0$, i.e. it represents the (series) resonance at f_s while the second one occurs when $\Gamma = 1$, or $z = \infty$, representing the anti–resonance at f_a. The outer–most circle corresponding to $|\Gamma| = 1$ describes a lossless impedance characteristic with pure inductance and capacitance. When losses, in the form of resistance, is present in the system, $|\Gamma|$ tends to be smaller than 1 and the circle tends to shrink. The amount of loss is indicated by the degree of shrinkage of the circle (Figure 2.8). On that contracted circle could there be smaller circles superimposing due to the sub–resonances named spurious modes which will be discussed in Chapter 3.

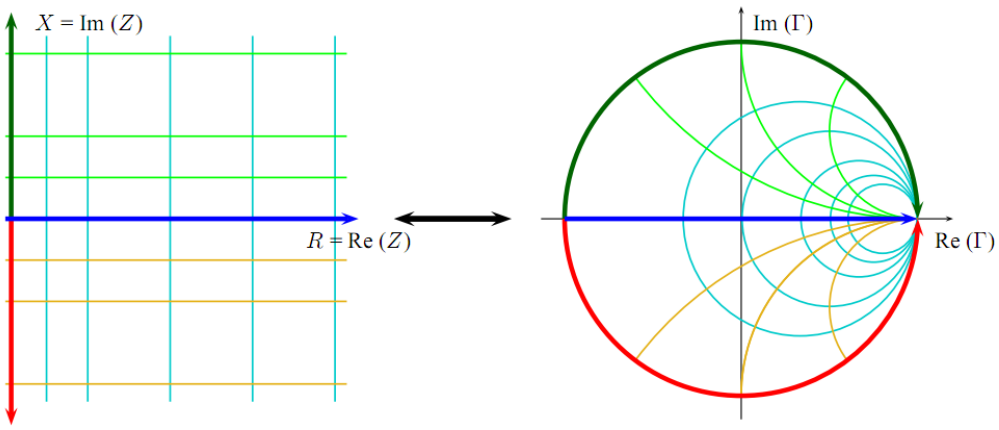

Figure 2.6. Transformation of complex impedance onto $\Gamma-$ plane [30]

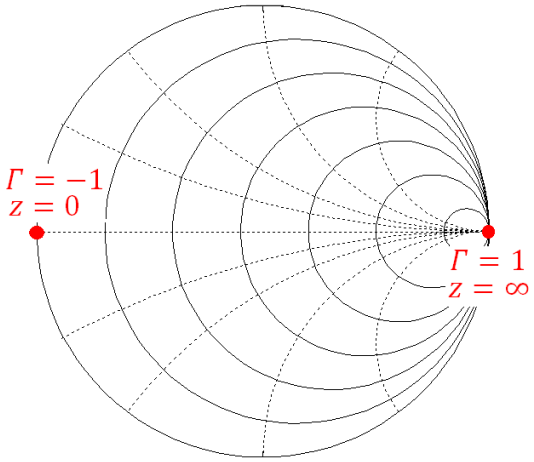

Figure 2.7. Two special points of the Smith chart

2.4 Performance Parameters

2.4.1 The Quality Factors

The quality factor by definition is the ratio of the total energy stored when the resonator vibrates at its resonance frequency to the total energy lost per cycle. In other word, the Q factor is a measure of degree of dissipation in a system. It indicates how well the energy is trapped inside a resonator during its cycles of operation. Therefore the higher the Q value is, the lower rate of energy loss.

$$Q = \omega \cdot \frac{total\ energy\ stored\ \ per\ \ circle}{energy\ loss\ \ per\ circle}$$

where $\omega = 2\pi f$ is the operating angular frequency of the FBAR device.
From this definition, the Q factor can be deduced from an equivalent mBVD circuit

$$Q = \frac{\omega}{2} \cdot \frac{C_m V^2 + C_0 V^2 + L_m I_2^2}{R_m I_2^2 + R_0 I_1^2 + R_s I_{total}^2} \tag{2.33}$$

Under an excitation, a resonator without loss experiences a non–decaying vibration at resonance frequency, consequently providing an infinite Q. However, in reality, due to the existence of many loss mechanisms, the degradation of Q factors is unavoidable. In a Smith chart, the Q factors are illustrated by the stretch of the $|\Gamma|$ circle as shown in Figure 2.8, so called the Q–circle of a resonator. Since the filter performance relates to Q factors, many efforts have been made to achieve as high Q of a resonator as possible.

As each resonator has a pair of operating frequency, the notation for Q factors at each frequency is specified. Q_r is defined as the quality factor at resonance and Q_a is that at anti–resonance. In some literature, they are also

written as Q_s for Q factor at series resonance and Q_p for Q factor at parallel resonance. There are at least four methods that are introduced to ascertain Q_r and Q_a [4, 28].

- The traditional 3–dB bandwidth method, in which Q_r is calculated by the full width half maximum (FWHM) of impedance Z at f_r and Q_a is computed by that of admittance Y at f_a

$$Q_r = \frac{f_r}{(\Delta f_r)_{3dB}} \quad ; \quad Q_a = \frac{f_a}{(\Delta f_a)_{3dB}} \tag{2.34}$$

- Using phase derivative of the impedance

$$Q_r = \frac{f_r}{2}\left|\frac{d\phi}{df}\right|_{f=f_r} \quad ; \quad Q_a = \frac{f_a}{2}\left|\frac{d\phi}{df}\right|_{f=f_a} \tag{2.35}$$

- Bode methods, which provides a formula to determine Q at any frequency of interest

$$Q(f) = 2\pi f * \tau(f)\frac{|S_{11}|}{1-|S_{11}|^2} \tag{2.36}$$

  where $\tau(f)$ is the group delay of element S_{11} of the scattering matrix.

- Extracting Q from a mBVD fitting circuit where

$$Q_r \approx \frac{2\pi f_s L_m}{R_s + R_m} \quad ; \quad Q_a \approx \frac{2\pi f_a L_m}{R_0 + R_m} \tag{2.37}$$

Each method has its own advantages and disadvantages, hence the choice of appropriate method depends on the applications as well as author preferences.

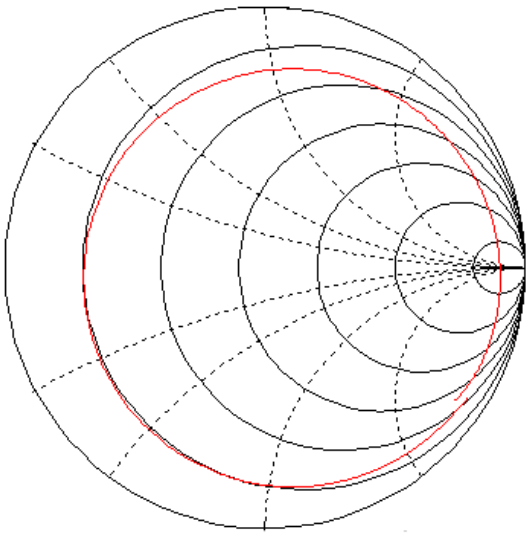

Figure 2.8. A Q–circle on the Smith chart

2.4.2 The Effective Coupling Coefficient

The effective coupling coefficient k_{eff}^2 is another key parameter that makes an impact on the filter performance. In FBAR, k_{eff}^2 expresses the strength of coupling between electrical energy and acoustic energy. By calculation, k_{eff}^2 is a relative measure of f_r and f_a that depend on the piezoelectric and electrode materials, the thickness ratio between these layers or the surface on which the piezoelectric layer is deposited. In (2.37) is the coupling of nth mode introduced [23, 27]

$$k_{eff,n}^2 = \frac{8k_t^2}{[(2n+1)\pi]^2} \tag{2.38}$$

Substitute k_t^2 in (2.29) into (2.36), gives

$$k_{eff,n}^2 = \frac{8k_t^2}{[(2n+1)\pi]^2} \Rightarrow k_{eff}^2 = k_{eff,0}^2 = \frac{8k_t^2}{\pi^2} \approx \frac{\pi^2}{4}\frac{f_r}{f_a}\frac{f_a - f_r}{f_a} \tag{2.39}$$

By which the bandwidth BW of the resonator is defined

$$BW = \frac{f_a - f_r}{f_a} \tag{2.40}$$

According to [28], the maximum BW and k_{eff}^2 that can be achieved with the best stack design and advanced AlN film growth is 2.8% and 6.9%, respectively. It is also stated that an effective coupling factor of 6.9% can satisfy most mobile communication applications.

2.4.3 FBAR in a Ladder Type Filter

The ladder is a type of configuration that comprises at least a shunt and a series resonator to create a filter. A simple ladder filter has several series and shunt FBARs as shown in Figure 2.9 (a). In the filter, all series resonators have the same resonance and anti–resonance frequencies. This is similar for all the shunt resonators. With this configuration, the filter center frequency falls within the anti–resonance frequency of the shunt resonators and the resonance frequency of the series resonators as in Figure 2.9 (b). The series resonators must have high Q factor at their resonance frequency and the shunt ones must have high Q at their anti–resonance frequency. The FBAR technology is hence forced to give high Q factors at both resonances.

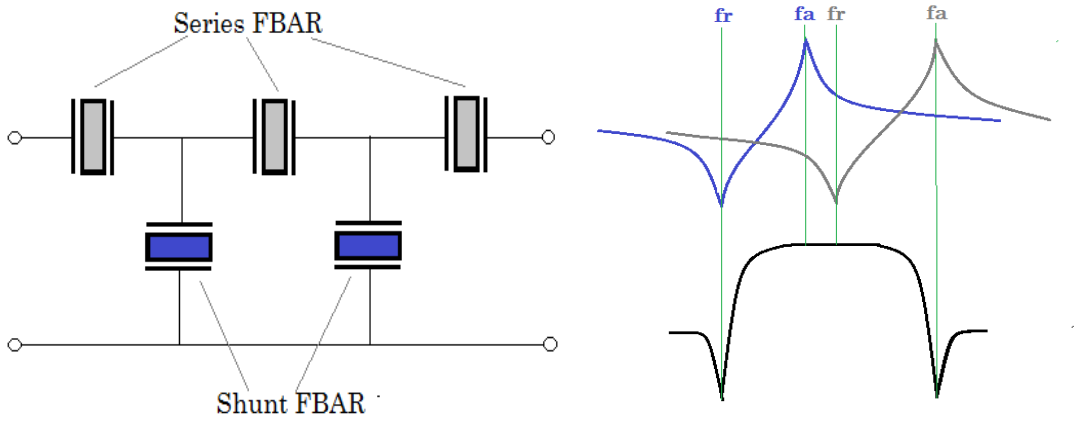

(a) (b)

Figure 2.9. Ladder filter (a) and its response (b)

2.4.4 The Impact of Key Parameters on The Filter Response

In order to study the effect of Q factors and k_{eff}^2 on the filter response, several definitions need to be declared.

- Insertion loss – the amount of energy inevitably absorbed by the filter.
- Bandwidth – the frequency range that can be passed by the filter.
- Selectivity – the measure of how efficiently the signal is attenuated across a range of frequencies. The selectivity is visualized by the steepness of the passband skirts in a filter response.
- Attenuation – the measure of how effectively the filter filters out unexpected frequencies. In other word, it is the difference in attenuation between passband and stopband (Figure 2.10).

With a given k_{eff}^2, higher Q_r and Q_a value means steeper filter skirts, thus gives a lower filter insertion loss and better filter selectivity. On the other hand, with fixed values of Q_r and Q_a, a larger k_{eff}^2 provides a larger separation between f_r and f_a, hence gives a wider 3–dB pass bandwidth which is required in some special applications. In Figure 2.11 is the effect of Q_a and k_{eff}^2 on a filter response shown. The k_{eff}^2 can be traded off for the increase of either Q_r or Q_a. For instance, a thicker electrode helps improve Q_r by reducing ohmic loss, yet results in a smaller k_{eff}^2. For this reason, there exists another definition for filter performance evaluation – the figure of merit (FOM) where

$$FOM = k_{eff}^2 * Q(f) \tag{2.41}$$

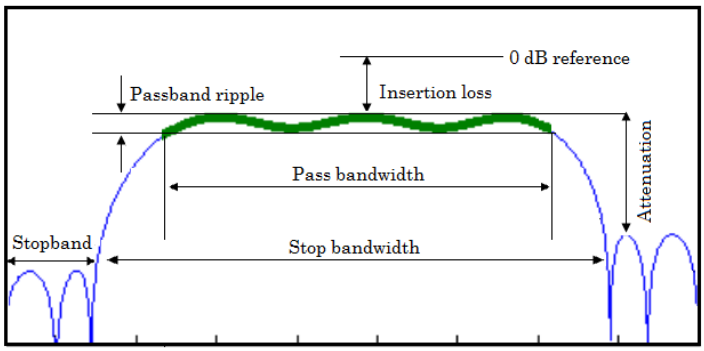

Figure 2.10. Example of a filter response

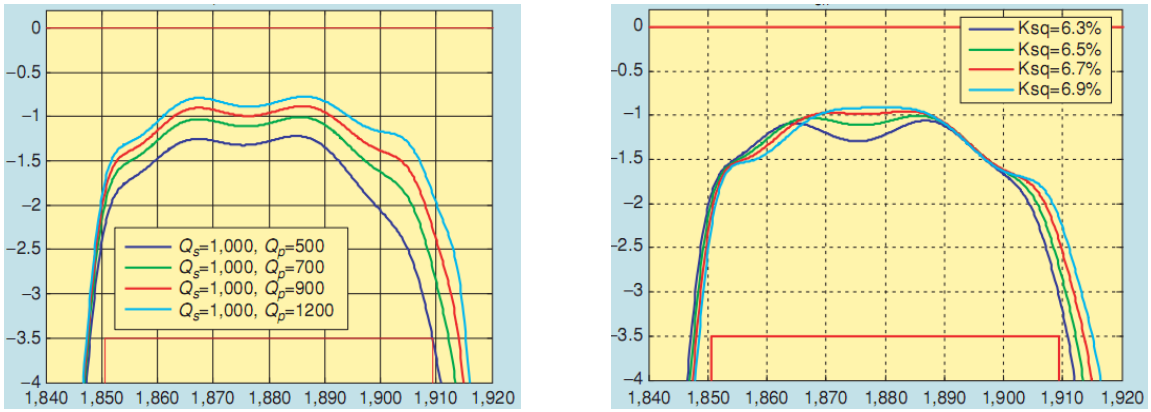

(a) (b)

Figure 2.11. The effect of Q_a (a) and k_{eff}^2 (b) on a filter response [28]

2.5 Sources of Q loss in FBAR

2.5.1 Lateral Leaking Waves

Unlike SMR, both the upper and lower surface of an FBAR are in contact with air. The leakage of waves in vertical direction is thus negligible since waves are reflected back at these surfaces due to large acoustic impedance mismatch. However, in lateral dimension, traveling Lamb modes (sometimes referred to as lateral modes) arising from the coupling between the main modes to the other ones laterally escape from the resonator. This happens due to the discontinuity of stress contribution at the perimeter of the resonator, making waves leak to the outside region and be lost, consequently lowering the Q value. In the mBVD circuit (Figure 2.5), this type of loss appears in the form of R_0. The amount of lateral leaking energy in a practical resonator, unfortunately, can be neither estimated by electrical measurement nor by laser interferometry [23]. Lateral leaking waves can be trapped inside the active region of the resonator by appropriate technique. However, a confinement of these waves comes with a rate. That is the trapping waves may vibrate and form standing waves in lateral

direction, thus either create more out–of–band spurious resonances or make the existing rattles worse [23]. Chapter 3 will provide an insight about this source of loss as well as the method to overcome the problem.

2.5.2 Acoustical Attenuation

Acoustical attenuation mechanism is caused by thermal–elastic phenomenon in which part of acoustical energy propagating in a material is converted into heat. The attenuation of acoustic waves also arises from viscous losses and impurity scattering. The effect is modeled by using complex propagation constant and in the mBVD circuit, it appears in the form of R_m.

2.5.3 Ohmic loss

Ohmic loss refers to both the resistive loss (represented by R_s in the mBVD circuit) and the ohmic dissipation. The former one is due to the electrode resistance and is the most pronounced near the operating point where electrical current is the largest [23]. The later dissipation is caused by non–flat stress distribution at operating frequency. This non–uniformity strongly associates with the spurious modes caused by symmetric Lamb modes. These spurious modes make the resonator vibrate at different amplitudes in different local areas. Since the displacement is equivalent to the voltage via piezoelectric effect, there will be voltage differences in various electrode areas. The potentials between these areas result in the current redistributions – or eddy currents, and thus, loss. This type of loss appears in the form of R_0 in the mBVD circuit.

2.6 Chapter Summary

This chapter has outlined the basic topics on modeling an FBAR in theory, including the wave equation and the solutions to it as well as the effect of piezoelectricity on the resonator operation. It also shows how to characterize the electrical impedance of a resonator, how to evaluate its performance as well as introduces the possible loss mechanisms existing in the system which explains for the degradation of the resonator quality factors and effective coupling factor.

CHAPTER 3. Lateral Standing Waves – Causes, Effects and Solutions

3.1 Excitation of the Lamb Waves

The propagation of acoustic waves in the previous chapter is analyzed in one dimensional manner based on the assumption that the resonator is finite only in its thickness direction. Since the lateral dimensions were assumed to be infinite, the effects of lateral boundaries on the resonator operation were ignored. However, this is untrue as in reality, the electrodes and piezoelectric layer are truncated for a small size device. The resonator is thus finite in all directions. This is the source for other types of wave and their effects arising in the system.

Longitudinal and shear bulk waves traveling through the thickness of the FBAR are reflected when encountering either the top or bottom electrode. Only in perpendicular incidence do they reflect back as pure bulk. In fact, these waves always deviate from the normal angle due to the anisotropic piezo–layer and the imperfection of the layer stack. In such an event, the waves will experience the "mode conversion" phenomenon, e.g. a longitudinal wave will convert into four different waves including transmitted and reflected longitudinal and shear waves [23]. The reflected longitudinal and shear waves are repeatedly converted upon reflections at any interfaces[2]. At a certain incident angle, these two waves will couple and recombine. In other words, they recreate themselves and periodically travel along the lateral, or x direction (y direction is omitted for simplicity). These waves are known as plate waves, or Lamb waves. The FBAR, supposing to be a waveguide for the fundamental longitudinal wave in z direction, is also a waveguide for Lamb waves in x direction. Each of the Lamb waves is an eigen–solution to the wave equation in this direction[3] and is called a mode. These modes, though have the same z component of the propagation constant (k_z) [31], they have different k_x values. This is a very important property for the construction of the dispersion diagram – the key feature of this thesis.

The Lamb modes are categorized into symmetric and anti–symmetric modes depending on the symmetry of their displacement profile with respect to

[2] Top and bottom electrodes as well as lateral edges.

[3] i.e. it is proportional to $e^{-jk_x x}$

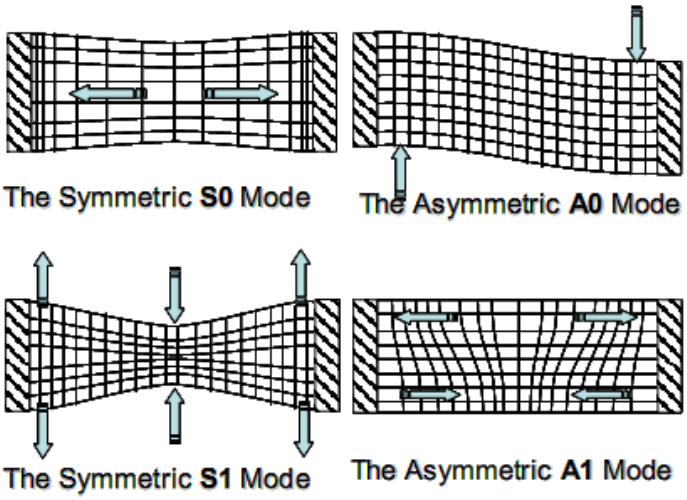

Figure 3.1. Particle displacement for the four lowest Lamb modes [10].

the middle plane of the plate. The symmetric ones are labeled as S_m and the anti–symmetric ones are labeled as A_m where m is the mode order. The displacement pattern for four lowest Lamb modes S_0, S_1, A_0, A_1 are depicted in Figure 3.1.

3.2 Dispersion Diagram

3.2.1 Dispersion Diagram of the Lamb Waves

Lamb modes propagating in a plate that has thickness of $2h$ always satisfy the Rayleigh–Lamb (RL) frequency equations [32], in which

$$\frac{\tan(qh)}{\tan(ph)} = -\frac{4k_x^{\,2}pq}{(q^2-k_x^{\,2})^2} \quad \text{for symmetric modes} \tag{3.1}$$

and

$$\frac{\tan(qh)}{\tan(ph)} = -\frac{(q^2-k_x^{\,2})^2}{4k_x^{\,2}pq} \quad \text{for anti–symmetric modes} \tag{3.2}$$

Two variables p and q are given by

$$p^2 = \left(\frac{\omega}{v_L}\right)^2 - k_x^{\,2} \text{ and } q^2 = \left(\frac{\omega}{v_S}\right)^2 - k_x^{\,2} \tag{3.3}$$

where k_x is the wave number[4], ω is the angular frequency, v_L and v_S are longitudinal and shear wave velocity, respectively. The equations (3.1), (3.2) and (3.3) can be solved for the dispersion relation k_x–ω of the Lamb modes. It can be written in the form

$$k_x = \frac{2\pi}{\lambda_{RL}} = \frac{2\pi f}{v_{RL}} = \frac{\omega}{v_{RL}} \tag{3.4}$$

[4] Lateral propagation constant.

here λ_{RL} and v_{RL} are the wavelength and wave velocity of Lamb modes. From the equations, several important points can be deduced

1. The Lamb waves originate from the combination of longitudinal and shear waves travelling in x direction, therefore, their phase velocities depend on the velocities of those two other waves.
2. When one analyzes the dispersion relation of a plate, only the thickness of the plate is matter. The width of the plate has no contribution to the wave velocities of Lamb modes.
3. The equations may have pure real, pure imaginary or complex solutions (k_x values). When the dispersion curves are plotted, the real solutions are more concerned as they present the propagation of the waves without attenuation. These waves are able to travel to the outside regions.

The dispersion diagram is a graph representing the relation of the wave modes and the frequencies upon which they disperse, or simply it is the wave number plotted as a function of frequency. In case of the four first Lamb waves, the diagram represents them as different dispersion curves characterized by their lateral wave numbers. Each curve is associated to a displacement profile as shown in Figure 3.2.

At higher frequencies, higher order Lamb modes exist but are weakly coupled so only the low order modes can be indicated [33]. The S_0 and A_0 modes normally originate at zero frequency. The frequencies at which the wave numbers of the modes reach zero are called the waveguide mode cut–off frequencies. One interesting finding is that the cut–off frequency of S_1 mode coincides with the resonance frequency of the main mode. This is the point where the fundamental mode is the strongest and its coupling with lateral modes is the

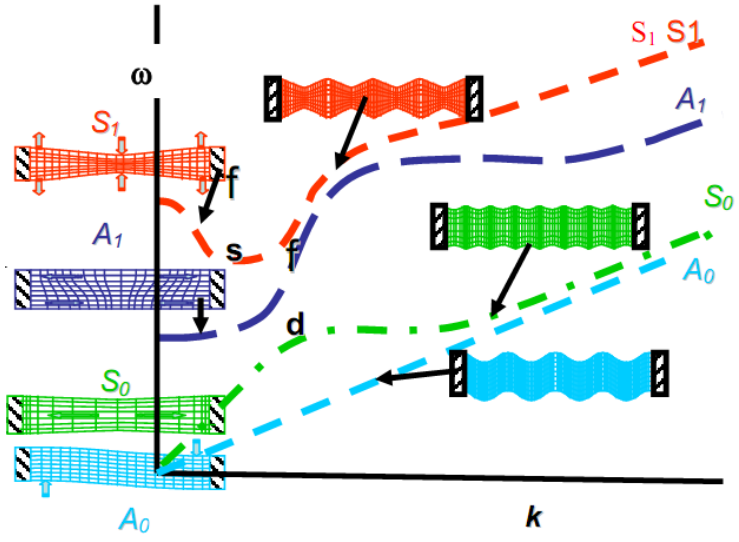

Figure 3.2. Dispersion diagram of the first four Lamb modes [33]

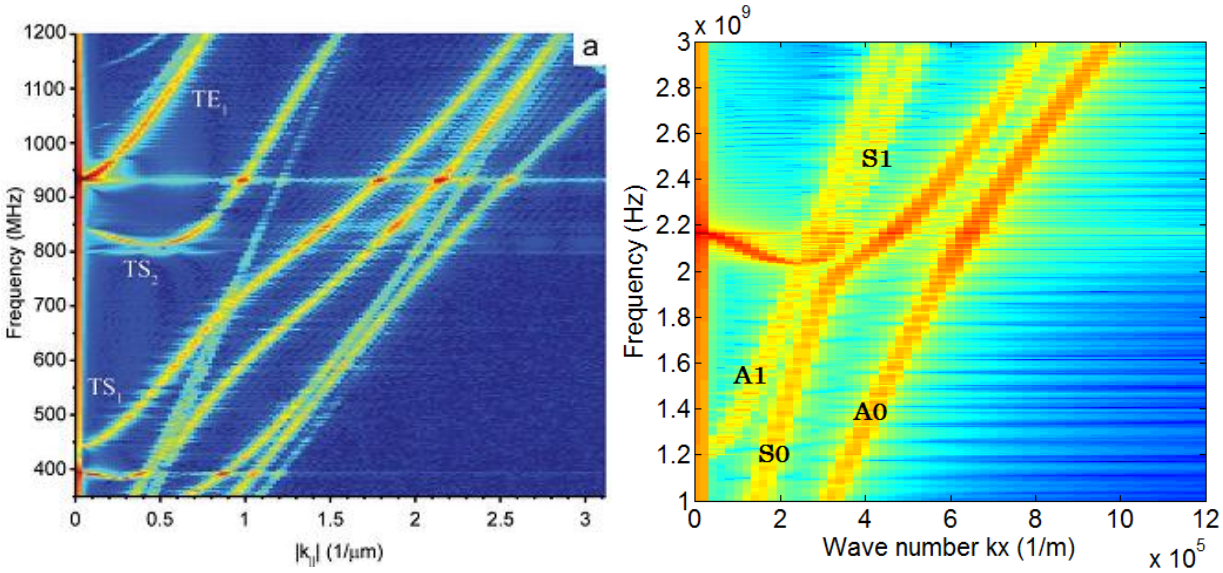

(a) (b)

Figure 3.3. Dispersion diagram of a ZnO–based SMR (a) [34] and a simulated AlN–based FBAR (b)

weakest because the contribution of the S_1 mode left branch to the total displacement disappears. It is also known as the piston mode in which the displacement profile is flat over the electrode area. The left branch of S_1 mode is identified as the strongest and the most easily excited mode – the reason why it is considered contributing the most to losses especially at the frequencies below f_s. The frequency corresponding to the lowest point in the S_1 curve is defined as the "dilatation" frequency. At this point, the mode bifurcates into two branches. The left branch has a negative group velocity[5] which is the particularity for a Type II dispersion. Figure 3.3 shows the dispersion curves plotted for Type I and Type II resonators. An FBAR with AlN as the piezoelectric layer supports a Type II dispersion while a resonator with ZnO piezoelectric layer has a Type I dispersion. For this type, the group velocity of S_1 mode is positive. In Figure 3.3, the modes TE_1, TS_1 and TS_2 are the alternative names for S_1, A_1 and A_2, respectively.

3.2.2 Method to Extract the Dispersion Diagram

There are several ways to determine the dispersion of the Lamb modes listed in [35]. One of the methods is by means of Discrete Fourier Transform (DFT) provided that the waves measured through either a time history or a

[5] Group velocity is the speed of the accumulated amplitude of a group of waves with different velocities. In a dispersion diagram, negative group velocities are illustrated by the negative slopes of the curves, likewise for the positive group velocity.

range of frequencies at uniformly spaced position along the propagation path are given. To obtain the dispersion, it needs a 2D DFT[6] for the time history case and only 1D DFT for the other circumstance. When the DFT is applied for a function of position x, it will be a function of the inverse wavelength[7] [35, 36]. Considering the later case, given that we have a data set of out–of–plane displacement u_z that is measured at N equally spaced positions along the x direction of a plate at each frequency. The plate is L wide. The dispersion relation can be written in the form

$$U(k_x, f) = DFT[u_z(x, f)] = \Delta \sum_{p=0}^{N-1} u_{z_p}(x, f) e^{-2\pi j k_n x_p} \tag{3.5}$$

where $x_p = p\Delta$ is the position, $\Delta = L/N$ is the space between two positions, and $k_n = n/L$ in which $n \in \left[-N/2; N/2\right]$ is the wave number in cycles per meter unit. The achieved $U(k_x, f)$ has complex values. The plot of its magnitude with respect to both k_x and f will be the desired dispersion diagram of the Lamb waves.

The DFT assumes that the signal consists of periodical data blocks and its computation is repeatedly implemented for only one identical block. Unfortunately, the u_z signal to which the DFT is applied is a block of non–periodic data, i.e. there will be a mismatch between the end of one sequence and the beginning of the next sequence. The transformation thus subjects to an effect named ”leakage” where the acquired Lamb modes smear out and have smaller amplitudes than expected. To diminish the leakage, a window function is utilized in advance to the DFT. This windowing will force two ends of the data block to zero and make it behave as a periodic signal. There are many available windows – Blackman, Flat top, Hanning, Hamming, Kaiser–Bessel, Welch, etc... However, wrong selection of the window might lead to more errors in the DFT spectrum. For the randomly distributed u_z data, it is recommended to use the Hanning window [37].

3.3 Effects of Lamb Waves on the Resonator Performance

As any other mechanical waves, Lamb waves propagating in lateral dimension also carry energy. When these waves encounter the border region of the top electrode, part of them reflect back and part of them escape to the outside region causing energy leakage. The problem arises since at the border, the

[6] Two dimensional DFT

[7] Inverse wavelength is another name for wave number k_x but is computed in cycles per meter rather than in radians per meter unit.

mechanical boundary condition requires vanishing of stress in the side of outside region but at the same time, the stress is still present in the side of active region. However, this requirement does not satisfy the condition of displacement continuity. Therefore, there must be a transition of the stress level from active region to outside region which is mainly the source of leakage (see Figure 3.4). The leakage appears in the form of mechanical waves in the vicinity of the resonator border region and is quite evident under an interfereometer as shown in Figure 3.5. In case of the FBAR, this leakage is dominant at certain frequencies and it is not easy to evaluate the amount of energy that is carried away from the resonator by the leaking waves. This problem has a negative effect on the resonator performance. The loss of energy not only degrades the Q factors but also affects the effectiveness of energy coupling. For this reason, designing a structure which is able to trap the lateral waves, preventing them from escaping out of the active region is an urgent mission.

As one mentions about the effect of Lamb waves towards FBAR performance, there is another consequence that should be taken into account – the spurious resonances. Since the resonator is laterally bounded, at certain frequencies, the Lamb waves fulfill the transverse resonance condition and form lateral standing waves. Consequently, in the impedance curve, smaller resonances emerge together with the main resonance of the fundamental mode (Figure 3.6). These satellite resonances are thus called the spurious modes. In a Smith chart, they are illustrated by the small circles superimposing on the main one. An interesting property of these spurious modes is that for a resonator with dispersion of Type II, they are closely spaced below series resonance frequency f_s and are further separated at those frequencies above f_s. This is opposite in the case of a Type I dispersion. The property can also be observed in a Smith chart, the small circles mainly round up in the lower half of the chart for Type II and in the upper half for Type I as shown in Figure 3.7. The explanation can be carried out by firstly reviewing Figure 3.3. In (a), S_1 mode, considered to be the strongest spurious mode, appears at higher frequencies than f_s while in (b) this mode (the left branch) emerge at those frequencies below f_s. In means that the strongest spurious modes take place below f_s for a type II resonator. Also in (b), for the frequencies above f_s, the S_0, A_0, A_1 mode and the right branch of S_1 mode propagate, i.e. they are responsible for any leakage and spurious modes happening in this range.

The spurious modes steal energy from the main mode. This can make the resonator Q factors decrease [10]. For a filter constructed of bulk acoustic wave

resonators, these modes also take responsibility for the unwanted ripples in the passband of the filter which deteriorate its smoothness .

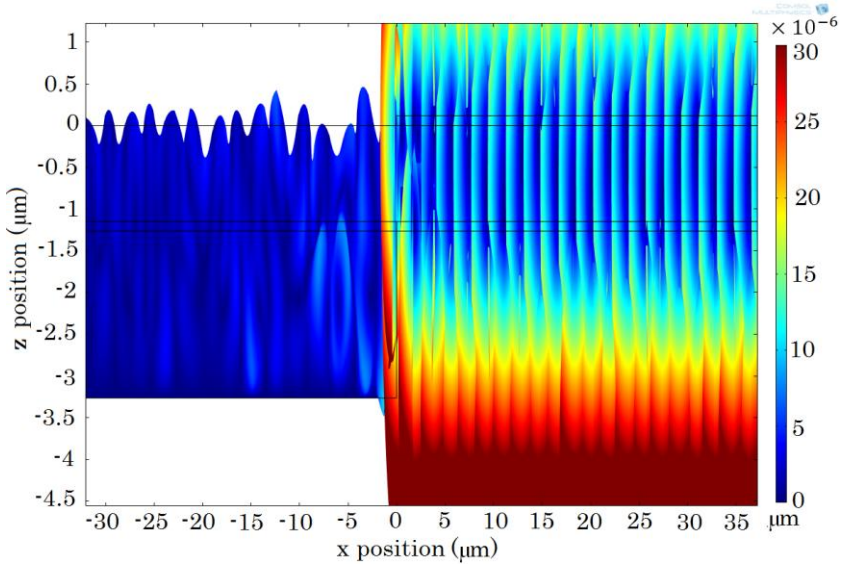

Figure 3.4. Displacement profile at the border region of a simulated FBAR at anti–resonance frequency

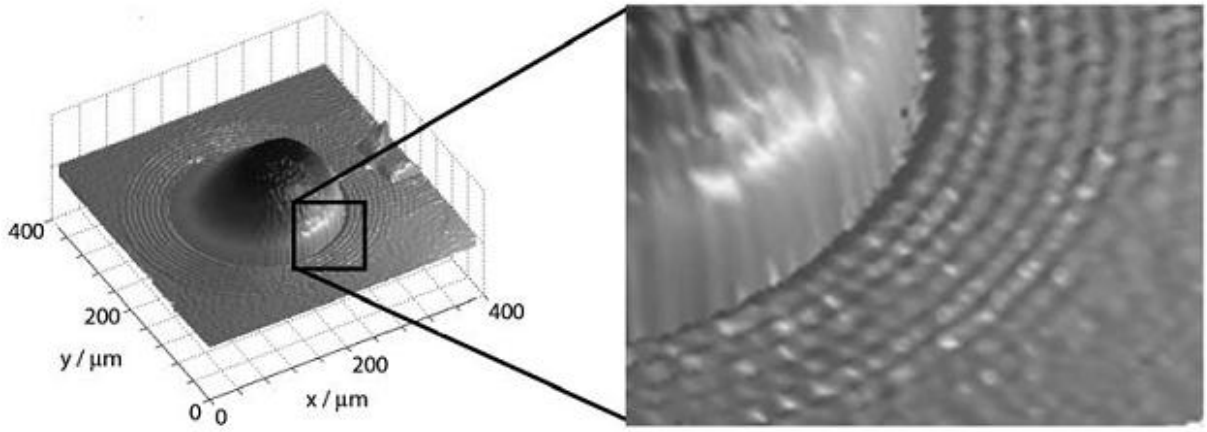

Figure 3.5. Interferometric measurement of laterally leaking waves in an SMR resonator device [23]

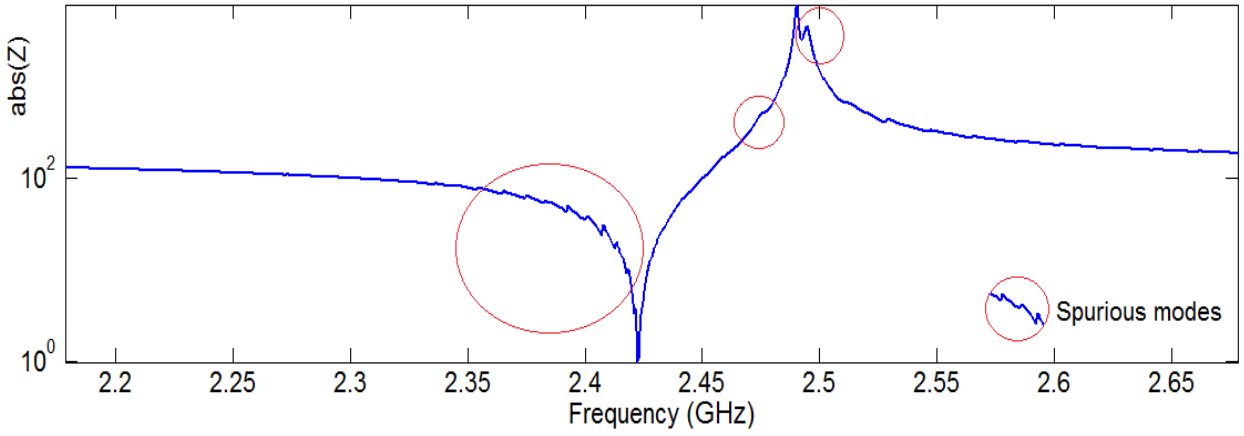

Figure 3.6. Parasitic spurious modes in electrical characteristic of the FBAR

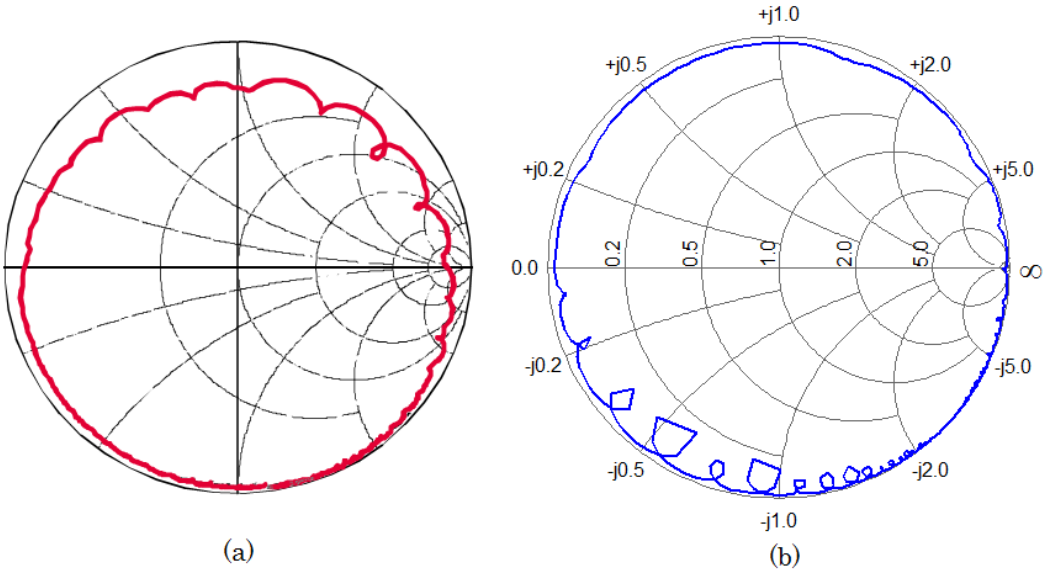

Figure 3.7. Spurious modes in a Smith chart plotted for a resonator with Type I [38] (a) and a simulated FBAR with Type II (b) dispersion[8].

3.4 Solution to Acoustic Leakage

The leakage occurs right at the top electrode border. One might wonder if there is a mechanism applied to this region so that it intercepts the leaking modes without negatively affecting the main mode. The answer is yes. It is called the frame method which is already reviewed briefly in the Introduction of this thesis. In this method, the material of interest will be added to the periphery of the top electrode to create a border region with different thickness (Figure 3.8). The presence of the frames was reported to give positive influence to the resonator performance. These frames perform as a lateral reflector that reflects Lamb waves back into the active region. To improve the reflectivity, the frame physics follow the Bragg's law adopted from optics, so–called the Acoustic Bragg Reflector (ABR).

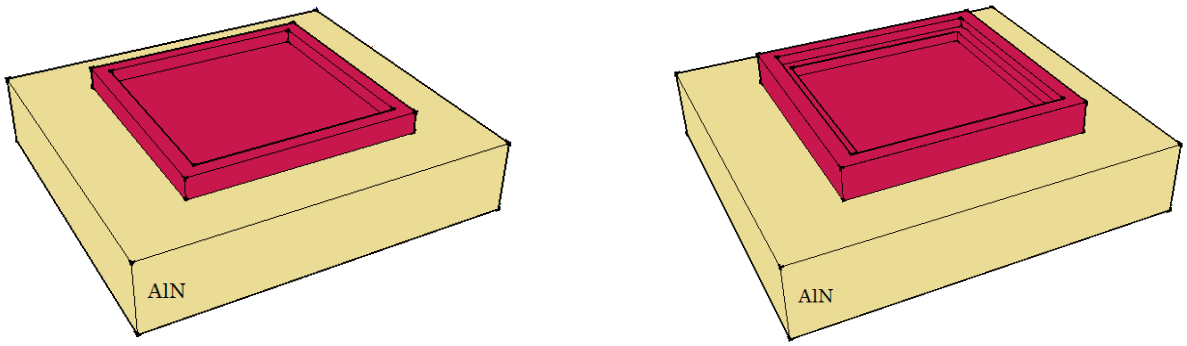

[8] The circles look like polygons due to the coarse discrete data set of frequencies.

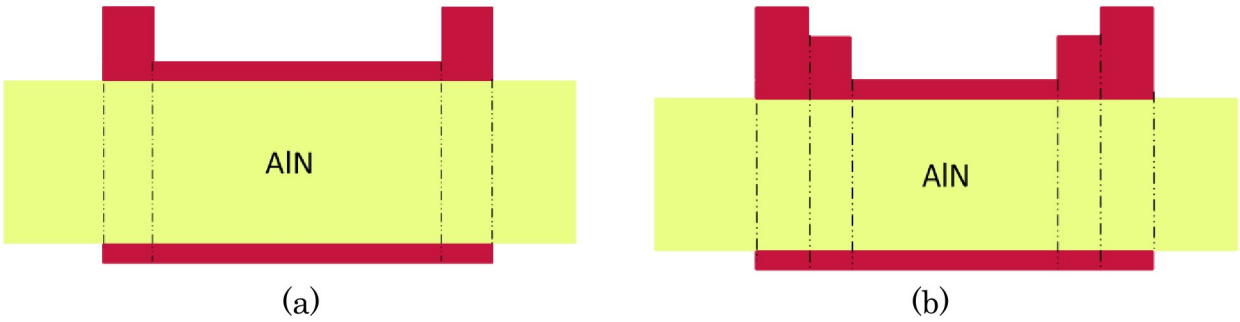

(a) (b)

Figure 3.8. 3D illustration (top figures) and 2D schematic (bottom figures) of the frame – one step design (a) and dual step design (b)

3.4.1 The Lateral Acoustic Bragg Reflector

A Bragg Reflector used in optics, as defined in [39], is designed with at least one dielectric mirror pair in order to reflect a radiation with a certain wavelength λ. Here the word "mirror" is used to indicate the reflection. Each mirror pair involves two layers with high and low dielectric materials as shown in Figure 3.9. The optical thickness of each layer has to be an odd multiple of a quarter of wavelength in order to form coherent superposition of the reflected waves [40]. Only in this way is the incident radiation effectively reflected back.

Compared to the Bragg miror used in optics, the principle of the ABR is of no different except that the light waves are replaced by acoustic waves and the mirror pair is now comprises two layers of high and low acoustic impedance materials. It is thus called the acoustic mirror pair. Assuming that the frames are made of the same material as the top electrode as in Figure 3.8, it is obvious that the acoustic wave velocity v_a is different for the various regions. Indeed, such thicker electrode shifts the dispersion curves downwards to the lower frequencies thus changing the wave numbers of all the modes (see Figure 3.10). Change in wave numbers means change in wave velocities. Deduced from equation (2.12), the condition for

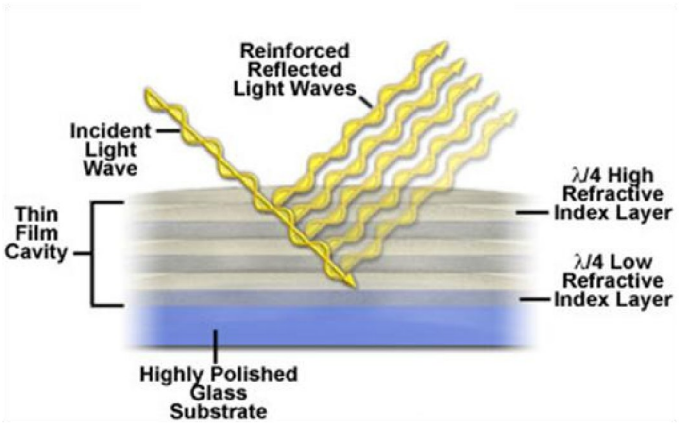

Figure 3.9. Illustration for dielectric mirror in optics [41]

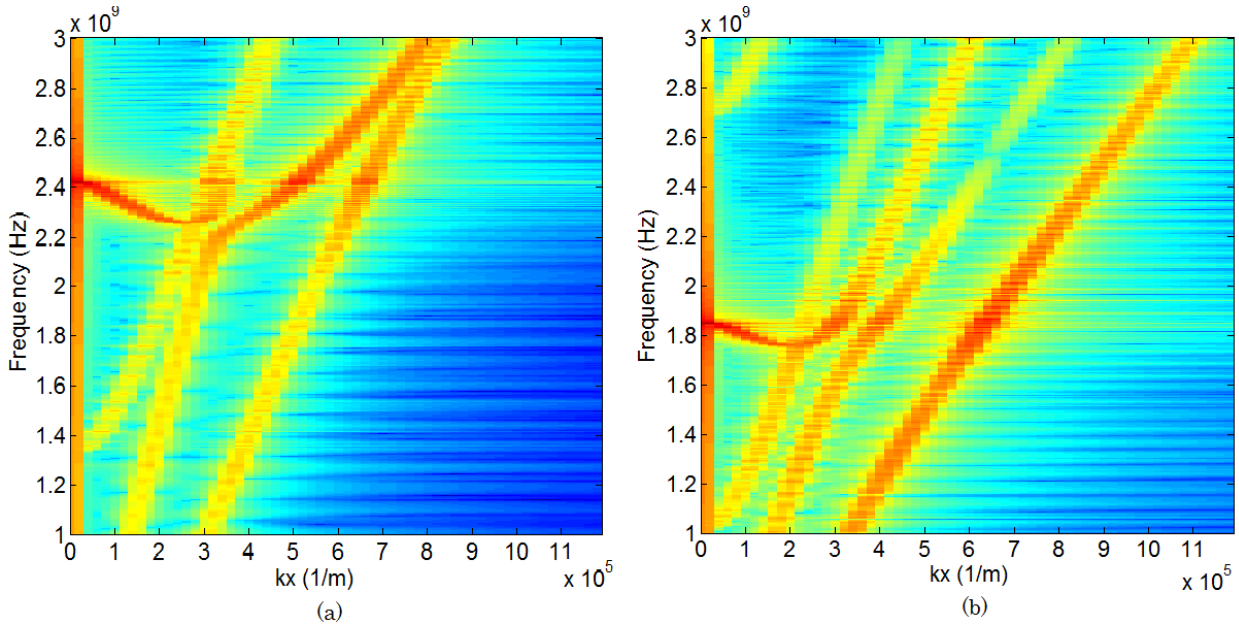

Figure 3.10. Dispersion diagram of for various thicknesses of the top electrode: 115 nm (a) and 403 nm (b)

different acoustic impedances is fulfilled. The border region now includes an ABR which is placed in lateral direction instead of thickness direction as it is used in SMR devices. The width of each individual frame, according to Bragg's law, is

$$W = (2m+1)\frac{\lambda}{4} \tag{3.6}$$

where m is a non–negative integer and λ is the wavelength of any plate waves.

3.4.2 Dual–Mode Reflection and the Diffraction Grating Method

The mentioned ABR designed based on (3.6) can only reflect one of the Lamb modes. If the frame width is calculated in a way that it is a multiple of the quarter wavelengths of two modes, it is able to reflect both of them at the same time. The idea of dual–mode reflection was published by S. Jose for optimizing the reflector stacks for SMR resonators. In her article [25], she introduced a method named the Diffraction Grating Method (DMG) which can be used to achieved the dual–mode reflection for thickness longitudinal and shear waves. This method will be modified and applied to the lateral ABR to reflect two modes that presumably have the largest contribution to the acoustic leakage – S_1 and S_0 mode.

The frame width computed for S_1 and S_0 modes are inherited from equation (3.6)

$$W(S_1) = (2m_1+1)\frac{\lambda(S_1)}{4} \tag{3.7}$$

$$W(S_0) = (2m_2 + 1)\frac{\lambda(S_0)}{4} \tag{3.8}$$

where m_1 and m_2 are positive integers.

$W(S_1)$ and $W(S_0)$ suppose to be equal, leading to following equations

$$(2m_1 + 1)\lambda(S_1) = (2m_2 + 1)\lambda(S_0) \tag{3.9}$$

$$\Leftrightarrow \quad (2m_1 + 1)\frac{1}{k_x(S_1)} = (2m_2 + 1)\frac{1}{k_x(S_0)} \tag{3.10}$$

$$\Leftrightarrow \quad (2m_1 + 1)k_x(S_0) = (2m_2 + 1)k_x(S_1) \tag{3.11}$$

$$\Leftrightarrow \quad m_2 = \frac{k_x(S_0)}{k_x(S_1)}m_1 + \frac{k_x(S_0)}{2k_x(S_1)} - \frac{1}{2} \tag{3.12}$$

Assume K is the ratio of S_0 mode's wave number and S_1 mode's wave number

$$K = \frac{k_x(S_0)}{k_x(S_1)} \tag{3.13}$$

Equation (1.8) can be rewritten

$$m_2 = Km_1 + \frac{K-1}{2} \tag{3.14}$$

The values of m_2 are calculated using (3.14) corresponding to positive values of m_1 such as 1, 2, 3… Since m_2 will never be an integer, it has to be rounded to the nearest integer number. The selection of m_2 follows two requirements

1. It has to be as near an integer as possible to minimize the error.
2. The rounded integer is as small as possible, or else the frame width will be unnecessarily too large due to the waste of material.

m_1 and m_2 are then substituted back to (3.7) and (3.8) to find the optimized frame width. Normally, $W(S_1)$ slightly deviates from $W(S_0)$ value due to the rounding procedure. Therefore, the optimum for one of the two reflected waves is not precise. If the frame width is the mean value of $W(S_1)$ and $W(S_0)$, both the modes are not optimum, but the error will be equally distributed.

3.5 Chapter Summary

This chapter provides basic knowledge about the formation and propagation of Lamb waves in the lateral direction. The method to extract their dispersion diagram is also presented. In an FBAR, these waves cause two essential problems – acoustic leakage and spurious resonances. This chapter focuses on finding the solution for the leakage problem. It is called the lateral ABR which is introduced to the basic FBAR in form of the frame located at the border region of the resonator. This frame is designed based on the understandings about dispersion curves and the DGM adopted from optics.

CHAPTER 4. Resonator Design

4.1 Material Selection

4.1.1 Piezoelectric Layer

The main concern for choosing piezoelectric materials involves high longitudinal acoustic velocity, low dielectric and acoustic losses, high electromechanical coupling coefficient, high thermal stability and the compatibility with new IC technology. In literature, materials such as aluminum nitride (AlN), zinc oxide (ZnO), lead zirconate titanate (PZT) have drawn attention as the piezoelectric layer for BAW resonators. These materials exhibit a considerably stronger piezoelectric effect, where their crystals deform under electrical excitation, compared to other piezoelectric materials, e.g. quartz crystal, cadmium sulfide (CdS), lithium niobate ($LiNbO_3$), barium titanate $(BaTiO)_3$. Among these materials, AlN is the most common one which can be deposited with stable and reliable process [38], providing high quality thin film for BAW devices. AlN is a binary compound with hexagonal wurtzite crystal structure which material properties are very stable at room temperature (thermal stability is kept up to 2200 degree celcius). The (002) oriented AlN film in which the c–axis is perpendicular to the substrate surface as depicted in Figure 4.1 is the most preferable material used in BAW resonator due to its highest piezoelectric stress constant in this direction.

AlN provides a typical piezoelectric coupling factor k_t^2 of 6.5%, and the maximum coupling of 6.9% is reported in [28] while ZnO offers a higher one, of about 8.5%. PZT provides even better k_t^2, value of 35% [23]. However, a good performance in term of coupling is the only property in which ZnO and PZT are

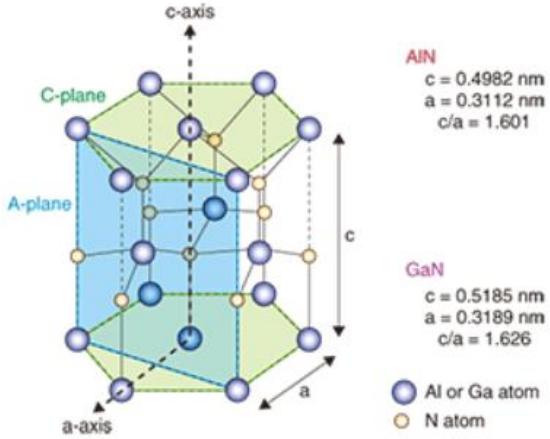

Figure 4.1. AlN crystal structure [42]

Table 4.1. Comparison of various piezoelectric materials [23, 43]

Material property	AlN	ZnO	PZT
Longitudinal acoustic velocity (m/s)	11050	6350	4600
Piezoelectric coupling factor (%)	6.5	8.5	35
Piezoelectric stress constant e_{33} (C/m^2)	1.55	1.32	~1000
Poisson ratio	0.246	0.387	0.31
Density (kg/m^3)	3260	5610	7500
Intrinsic loss	Very low	Low	High
CMOS compatibility	Yes	No	No
Crystal symmetry class	6mm	6mm	4mm

better than AlN. AlN, in return, has advantageous properties over both ZnO and PZT when considering other aspects, including an exceedingly high acoustic wave velocity in order to achieve a high Q and low absorption (imaginary part of β), low intrinsic losses at high frequency while ZnO and PZT exhibit poor acoustic velocity and high acoustic losses. Furthermore, AlN becomes easier to fabricate in mass volume whereas the other two confront higher manufacturing difficulties [38]. The comparison of these materials is summarized in Table 4.1 where material data are adopted from [23, 44].

A superior acoustic wave velocity, low loss, fairly high coupling coefficient, reliable fabrication process and the possibility for CMOS integration have made AlN a preferred material for BAW resonator in general, and in particular for the designed FBAR in this thesis.

The parameter sets for AlN are declared in term of matrices including stiffness (or elasticity) matrix, permittivity (or dielectric) matrix and piezoelectric constant matrix. The material parameters are adopted from [43]. The symmetry of the matrices is applied for hexagonal class crystal structure (6mm) following the one described in references [27, 45]

- Permittivity matrix

$$\begin{bmatrix} \varepsilon_{11} & 0 & 0 \\ 0 & \varepsilon_{11} & 0 \\ 0 & 0 & \varepsilon_{33} \end{bmatrix} \quad \text{where} \quad \begin{matrix} \varepsilon_{11} = 8 \\ \varepsilon_{33} = 9.5 \end{matrix} \quad (\times 10^{-11} F/m)$$

- Stiffness matrix

$$\begin{bmatrix} c_{11} & c_{12} & c_{13} & 0 & 0 & 0 \\ c_{12} & c_{11} & c_{13} & 0 & 0 & 0 \\ c_{13} & c_{13} & c_{33} & 0 & 0 & 0 \\ 0 & 0 & 0 & c_{44} & 0 & 0 \\ 0 & 0 & 0 & 0 & c_{44} & 0 \\ 0 & 0 & 0 & 0 & 0 & c_{66} \end{bmatrix} \quad \text{where} \quad \begin{aligned} c_{11} &= 3.45 \\ c_{12} &= 1.25 \\ c_{13} &= 1.20 \\ c_{33} &= 3.95 \\ c_{44} &= 1.18 \\ c_{66} &= 1.10 \end{aligned} \quad (\times 10^{11} N/m^2)$$

- Piezoelectric constant matrix

$$\begin{bmatrix} 0 & 0 & 0 & 0 & e_{15} & 0 \\ 0 & 0 & 0 & e_{15} & 0 & 0 \\ e_{31} & e_{31} & e_{33} & 0 & 0 & 0 \end{bmatrix} \quad \text{where} \quad \begin{aligned} e_{15} &= -0.48 \\ e_{31} &= -0.58 \\ e_{33} &= 1.55 \end{aligned} \quad (C/m^2)$$

In order to imitate the behavior of the real material, a mechanical damping ratio of 0.25% is included in the physical parameters specified for the AlN layer. Another material loss parameter that needs to be considered is dielectric loss, or electrical permittivity loss[9]. This value is reported ranging widely from 0.0005 to 0.01 [46]. In this work, the dielectric loss applied for the simulated material is initially 0.002 and will be varied to verify its effect on the Q factor.

4.1.2 Electrode Layers

The right selection of the material for electrode layers can help improve the effective coupling coefficient which can be directly translated into an enhanced filter bandwidth. This enhancement can be achieved by choosing a high acoustic impedance material [4]. The explanation for this is due to the improved match in the distribution of acoustic standing wave to the linear distribution of an applied electric potential [47]. Considering the requirement of a large acoustic impedance value, a group of metals are able to satisfy the requirement for the resonator electrodes including tungsten (W), molybdenum (Mo), platinum (Pt), ruthenium (Ru). Table 4.2 shows the important properties of these materials. Tungsten offers the highest acoustic impedance, which results in both the highest k_{eff}^2 and an excellent acoustic impedance ratio between AlN and the electrode material, helping confine the waves in the active region of the resonator and reduce acoustic leakage in vertical direction. The statement is

[9] Sometimes it is referred to as the loss tangent (tanδ).

clarified in both Figure 4.2 and Table 4.2. Taking advantage of this property, a layer stack W/AlN/W is applied for active region of the simulated FBAR in this thesis. A structural loss factor of 0.33% is also included in the physical properties of the simulated tungsten material. The summary of material loss factors used in the simulation is shown in Table 4.3. The mechanical loss factor of Si in the table is adopted from [48]

Table 4.2. Important properties of the candidate metals used to fabricate the resonator electrode [38]

Metal electrode property	W	Ru	Pt	Mo
Acoustic impedance ($\times 10^6$ kg/m^2.s)	101	73.4	69	63.1
Acoustic velocity (m/s)	5230	5970	3260	6250
Density (kg/m^3)	19350	12100	21460	10200

Table 4.3. Material loss factors

Material	Isotropic structural loss	Loss tangent
AlN	0.25%	0.002
W	0.33%	–
Si	5%	–

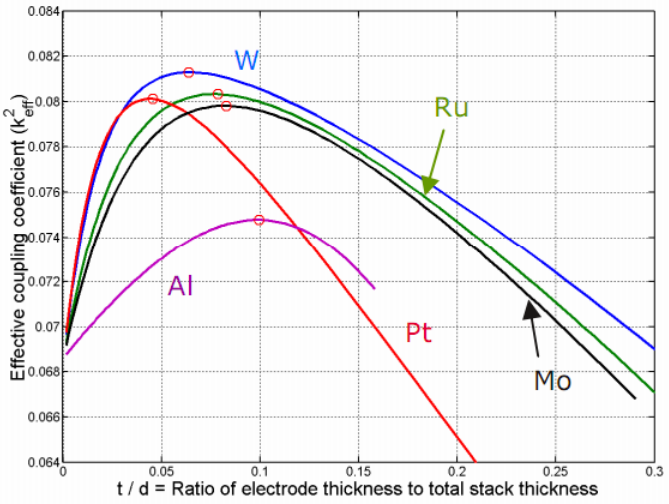

Figure 4.2. Comparison of k^2_{eff} of various electrode materials [38]

4.2 2–D FEM Simulation

In order to simulate the effect of plate waves towards the resonator performance, a 2–D model analysis of the FBAR device using Finite Element Method (FEM) is carried out by COMSOL Multiphysics® software. The schematic of the model is shown in Figure 4.3 with full representations of the geometry, dimensions, materials and boundary conditions. The silicon substrate

is partly truncated at the point that has negligible stress in order to reduce the amount of calculation. Symmetry is also applied in the model so the simulation is implemented for only a half of the FBAR for the same reason. Fixed constraint is applied to the bottom boundary of the FBAR. The device supposes to work in the air environment. However, the simulated one is covered by vacuum, which is the default setting of COMSOL. The justification for this substitution is that air has very low acoustic impedance, of around 0.0004 kg/m^2.s. The impedance mismatch of the materials of which the device is made and the air is assumed agreeing with the impedance mismatch of those materials and vacuum. Therefore it can be assumed that vacuum is a good approximation. The displacement field in the omitted dimension (u_y) is fixed to zero. Outside the active region, a 75μm–wide area of AlN placed on Si substrate is included in order to ensure that it could contain the evanescent tails of the waves trapped by the two electrodes, hence no critical boundaries appear near the active region. On the other hand, some non–trapping acoustic waves could reflect upon the edges of the outside region, forming standing waves in lateral direction and causing artificial satellite resonances to appear on the electrical behavior of the FBAR. This artificial effect is not found in the real device with a broad outside region. This source of error can be eliminated by adding Perfectly Matching Layers (PMLs) to the two sides of the resonator. In COMSOL, PML is an additional domain that is able to absorb the incident waves thus prevents any reflection upon its outer–most boundary, ensuring a fair agreement between the simulated and an actual FBAR. The PMLs used in this simulation are 5 μm wide. Electrical excitation is performed by setting an alternating voltage of 1V between the top and bottom electrode of the FBAR.

Mapped mesh is utilized in the simulation to control the element size in different regions. This meshing strategy is beneficial in calculating the dispersion diagram where the analysis of a uniformly spaced out–of–plane displacement (u_z) at a particular interface is required. The mesh size is set to maximum 100 nm in vertical direction, 1 μm for the outside region in lateral direction and 100 nm for the active region also in this direction.

Modal analysis is carried out over the frequency range from 1 GHz to 3 GHz, supposing to cover the main resonance, with the step size of 0.5 MHz. This step is smooth enough to capture other sub–resonances existing in the resonator electrical characteristic for further analyses and study.

The FBAR is designed so that it operates at about 2.4 GHz, falling within the S–band which covers the frequency range from 2 – 4 GHz according to IEEE

standard. The strong dependence of the resonance frequency on the W/AlN/W stack thickness and of k_{eff}^2 on the ratio of the electrode thickness and total stack thickness requires careful consideration in defining the thickness for each specific layer. Figure 4.4 shows the simulation results for k_{eff}^2 at various ratios of electrode and piezoelectric layer thickness. The operating frequency of the simulated resonator is in the vicinity of 2.4 GHz. k_{eff}^2 is calculated based on formula (2.39). From these results, thicknesses of *ht* =115 nm and *hpzd* =1150 nm (which ratio is 0.1) are assigned to each electrode and the piezoelectric layer, respectively, for future simulations.

The electrical behavior of the model is illustrated via the impedance curve plotted in Figure 4.5. According to the graph, resonance and anti–resonance frequency of the FBAR are found at $f_r = 2.4225$ GHz and $f_a = 2.4905$ GHz, respectively.

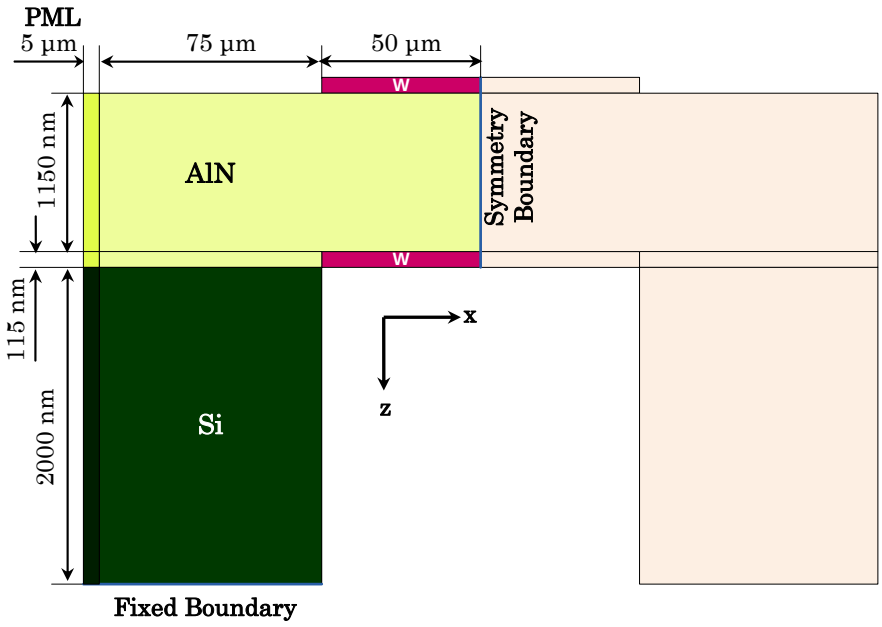

Figure 4.3. 2–D FEM model geometry of the FBAR without optimization

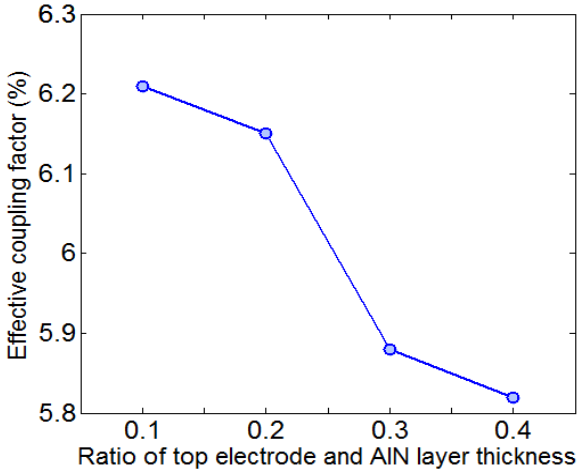

Figure 4.4. Effective coupling factor versus thickness ratio

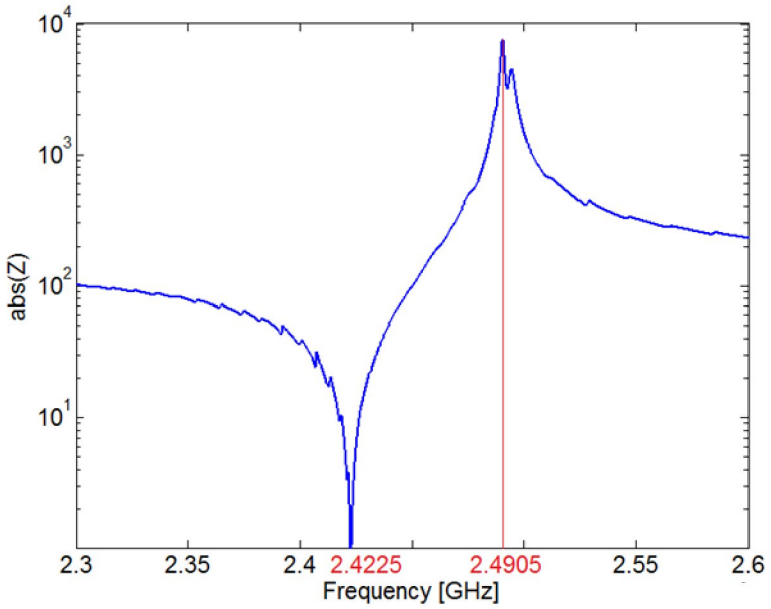

Figure 4.5. Resonance and anti–resonance frequency identified in the simulated response of an FBAR

4.3 Calculating the Dispersion Diagram

The complex values of out–of–plane displacement (u_z) array at the lower interface of the top electrode are exported from COMSOL and manipulated using MATLAB program (Appendix A). These values are uniformly spaced along x direction and is extracted for a particular region. For instance, according to the mesh setting of the FBAR in section 4.2, the uniform space for the active region is 100nm, so the length of the array is L = 501. A Hanning window with the length of 501 is applied to the array in order to reduce the leakage caused by the non–periodic u_z sequence. The dispersion diagram can be obtained by applying 1D FFT to this windowed array to transform the data from the spatial domain to the wave–number domain. Figure 4.6 and 4.7 (a) shows the dispersion diagrams plotted for the FBAR in Figure 4.3 for various thicknesses of the top electrode, e.g. 1.3 times ht (≈150 nm), 2.5 times ht (≈ 288 nm). The lateral wave–numbers of Lamb modes (depicted by the local maxima of the line graphs in Figure 4.6 and 4.7 (b)) are calculated at the resonance and anti–resonance frequency. These two electrode thicknesses will be assigned to the heights of the frames designed in the next section. It has to be noted that from here the structure shown in Figure 4.3 is going to be referred as the basic FBAR in this thesis.

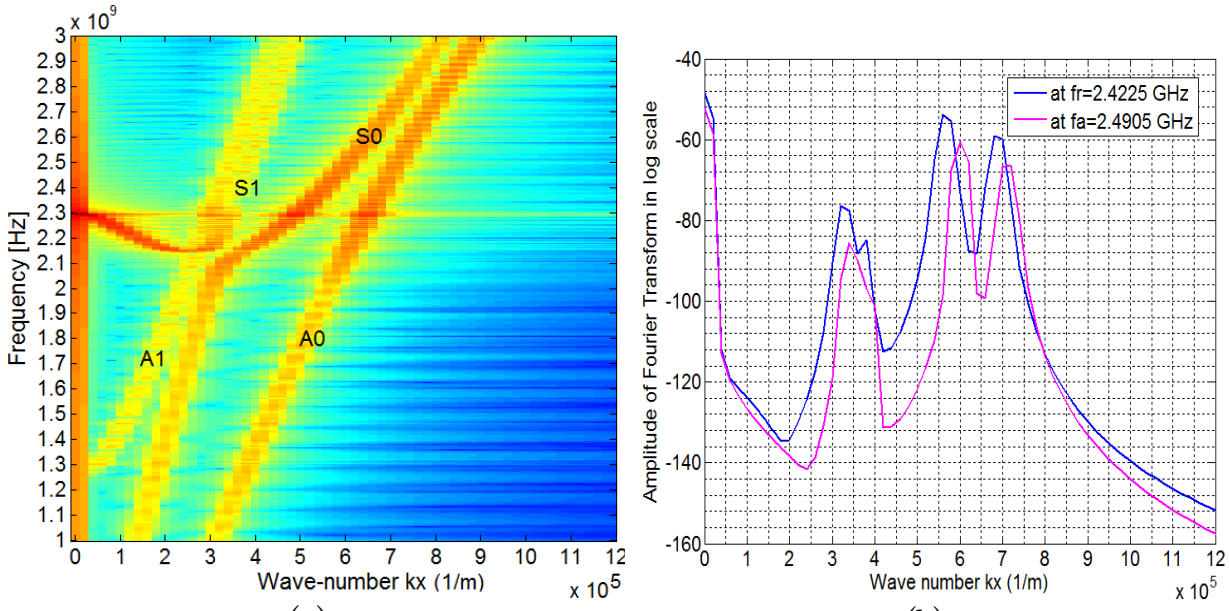

(a) (b)

Figure 4.6. Dispersion diagram plotted for the region with the top electrode thickness of 150 nm

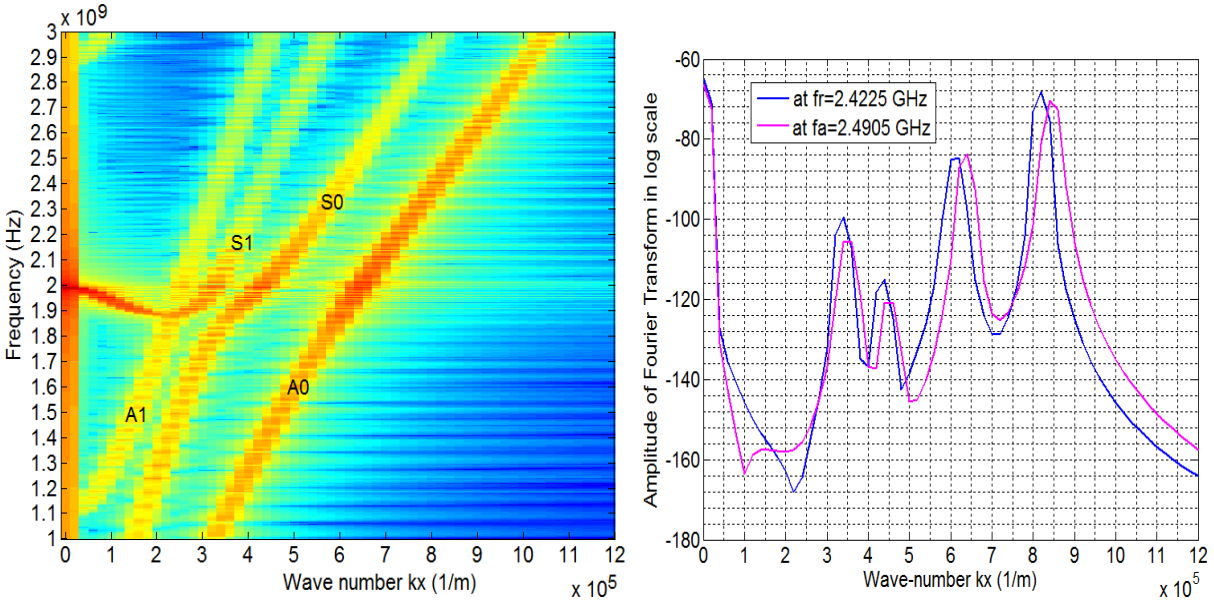

(a) (b)

Figure 4.7. Dispersion diagram plotted for the region with the top electrode thickness of 288 nm

The Q factor is supposed to be calculated and optimized for both resonance (Q_r) and anti–resonance frequency (Q_a). While Q_r can be improved by controlling the thickness of the top electrode, Q_a turns out to be more difficult to enhance. Indeed, the increase in the top electrode thickness leads to the reduction of ohmic loss and thus increases Q_r [28]. Therefore, this thesis will focus on optimizing the FBAR so that it offers as higher Q_a as possible. The lateral wave–

Table 4.4. Wave–number k_x (1/μm) of the first four Lamb modes at anti–resonance frequency calculated for various top electrode thicknesses

Top electrode thickness (nm)	A_1	S_1	S_0	A_0
150	0.34	0.39	0.60	0.71
288	0.35	0.45	0.64	0.85

Table 4.5. Quarter wavelengths (nm) of first four Lamb modes at anti–resonance calculated for various top electrode thicknesses

Top electrode thickness (nm)	A_1	S_1	S_0	A_0
150	735	641	417	352
288	714	556	391	294

number data from the dispersion diagrams are collected at anti–resonance frequency for this purpose, and are enumerated in Table 4.4. The corresponding quarter wavelengths of the Lamb modes are also provided in Table 4.5.

4.4 Designing of Border Region

4.4.1 FBAR with Single Frame for Dual–mode Reflection

As it was introduced in the previous sections, a frame is placed onto the periphery of the basic FBAR. The height of the designed frame is chosen to be 2.5 times the thickness of the top electrode because of several reasons:

1. This height provides a minimum error in determining the integer m_2 among various tested frame heights (Appendix B.1)
2. The step is large enough to bring a considerate variation in the quarter wavelength of each corresponding lateral wave between various regions (Appendix B.1).
3. Too huge step would negatively affect the boundary conditions between the different regions [17], i.e. the condition of continuity is not well satisfied. In addition, it might promote the stress concentration at the tip potentially resulting in mechanical failures in the device.

Its width is determined following the DGM described in sub–section 3.4.2. Based on the data in Table 4.4, the quarter wavelengths of the first four Lamb waves are found and shown in Table 4.5.

The implemented frame performs as a part of an acoustic Bragg mirror, reflecting Lamb waves back into the active region of the resonator and preventing them from leaking to the outside region. It is stated in [23] that the Q factors can be enhanced provided that the width of the frame is chosen to be

multiples of the quarter wavelength of S_1 mode, meaning that the frame will reflect only this mode. In order to promote the impact of the frame on Q factors, the one in this thesis is designed in such a manner that it reflects two specific modes: the zero (S_0) and first order (S_1) symmetric mode. Corresponding to the height of 288 nm, the quarter wavelengths are 714 nm and 391 nm for S_1 mode and S_0 mode, respectively. The ratio of lateral wave–number of S_0 and S_1 mode is

$$K = \frac{k_x(S_0)}{k_x(S_1)} = 1.422$$

Two integers m_1 and m_2 are found from (3.14). Since m_2 in Table 4.6 is not an integer, it is supposed to be approximated to the nearest integer. The most appropriate value for m_2 is the rounding number of 3.056, which is 3, and the corresponding value for m_1 is 2.

Based on equations (3.7) and (3.8), the corresponding width of the frame optimized for S_1 mode is 2780 nm and the one optimized for S_0 mode is 2737 nm. The deviation between two calculated widths is evident since m_2 itself is not precisely an integer. The error comes from the necessary rounding procedure. The width of the designed single frame for dual–mode reflection is chosen to be 2750 nm, as shown in Figure 4.8.

Table 4.6. Calculation for m_1 and m_2

m_1 (for S_1 mode)	1	2	3	4	5
m_2 (for S_0 mode)	1.633	3.056	4.478	5.900	7.322

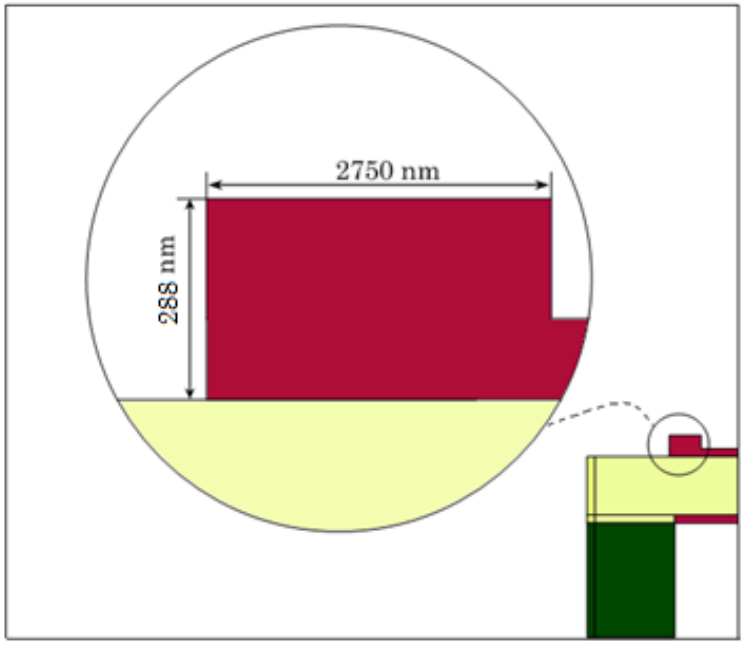

Figure 4.8. Schematic of the designed single–frame

4.4.2 FBAR with Dual Frame for Dual–mode Reflection

A dual frame can be achieved by adding another frame to the one already implemented in Figure 4.8. The height of the second frame is 130% of the top electrode thickness (or 150 nm). It is designed using the same procedure as for the first frame and is placed next to the inner boundary of it. Two integers m_3 and m_4 will be used instead of m_1 and m_2. m_3 corresponds to the frame width calculated for S_1 mode. m_4 corresponds to the one computed for S_0 mode. The ratio of lateral wave–number of S_0 and S_1 mode propagating in the second frame is

$$K' = \frac{k_x(S_0)}{k_x(S_1)} = 1.538$$

The calculation for m_3 and m_4 of the second frame is in Table 4.7.

According to Table 4.7, the appropriate value for m_4 is 2, and the corresponding value for m_3 is 1. The width of the second frame optimized for S_1 mode is 1923 nm and the one optimized for S_0 mode is 2085 nm. The width of the single frame is chosen to be 2000 nm. The schematic for the designed dual–frame for dual–mode reflection is shown in Figure 4.9.

Table 4.7. Calculation for m_3 and m_4

m_3 (for S_1 mode)	1	2	3	4	5
m_4 (for S_0 mode)	1.808	3.346	4.885	6.423	7.962

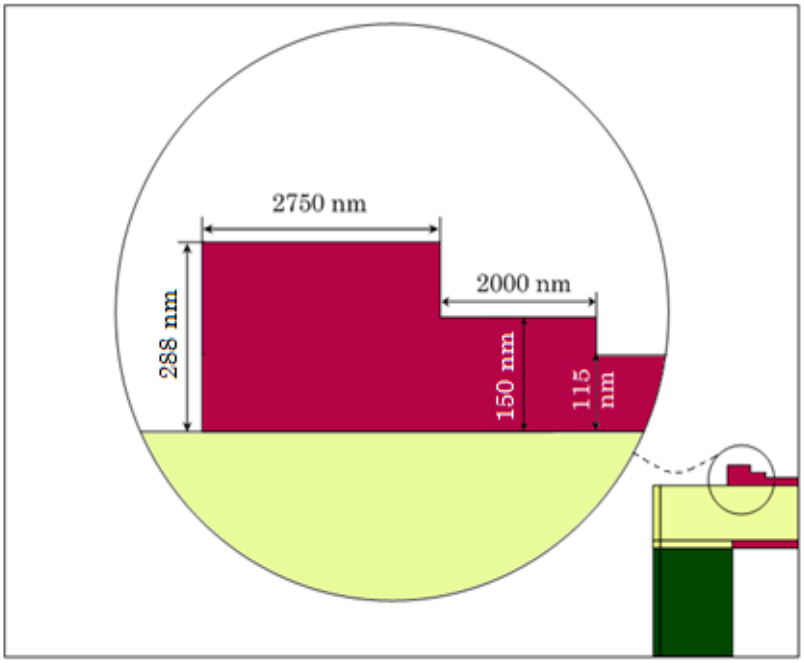

Figure 4.9. Schematic of the designed dual–frame

The FBAR with frames designed by implementing the mentioned method are carried out using COMSOL software. The Q factors are extracted from the achieved electrical characteristics. The calculation of Q factors follows (2.34) – the 3dB bandwidth method. Unlike practical measurements in which the measured frequencies and electrical impedance amplitude are easily affected by environment consequently giving incorrect 3dB bandwidth, the ones obtained from COMSOL are much more stable and precise thus providing reliable extraction of Q values.

4.4.3 FBAR with the Repeated Dual Frame

The ABR normally comprises more than one pair of acoustic mirrors, resulting in a structure with many alternative low and high acoustic impedance layers. The purpose of this multiple–pair structure is to enhance the reflectivity of the ABR. In case of lateral ABR, this can be done by repeating the dual frame configuration in the lateral dimension. An FBAR with two pairs of dual frame (Figure 4.10) is analyzed in COMSOL for the expectation of a more powerful frame structure and higher Q factors.

4.5 Chapter Summary

This chapter focuses on the design procedure for the FBAR structure. The materials for each layer, especially the piezoelectric layer, are carefully selected based on critical criteria such as facilitating the acoustic waves, low internal loss, high electromechanical coupling factor, IC circuit compatibility. The ratio of layer thickness is also considered for a good coupling factor. All of these standards are included in a COMSOL simulation model built in a way so that it is as close to reality as possible. Extracted information from the dispersion diagram is used to determine the optimized frames, following the methods recommended in Chapter 3. Three frame structures are carried out – a single step frame, a dual step frame and a repeated dual frame. The second one is the key design in this thesis.

Figure 4.10. Schematic of the FBAR with two pairs of acoustic mirrors

CHAPTER 5. Results and Discussions

5.1 Enhancement of Q factors

The Q factors are computed for various FBAR structures including the basic FBAR with no frame, the one with a single frame that can only reflect S1 mode and the ones designed for dual–mode reflection. The comparison of the Q factors of these structures is shown in Table 5.1 and is graphically illustrated in Figure 5.1 where the electrical impedance amplitude and phase are presented. Figure 5.2 shows the Smith chart plotted for the FBAR with a single frame designed for dual–mode reflection and the one with a dual frame compared to the basic FBAR. The spurious modes are well represented in the left graph. In the right graph, part of the Q circles near the point presenting anti–resonance is depicted.

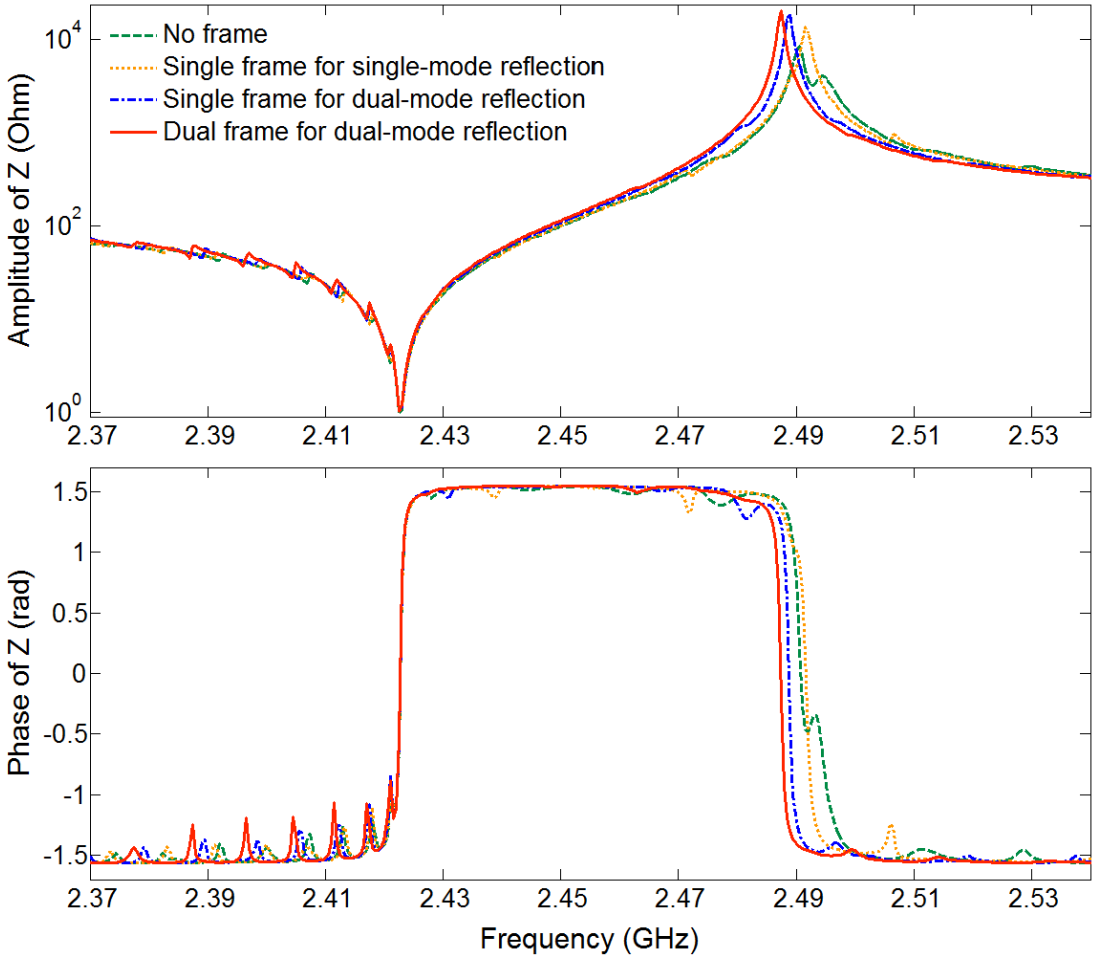

Figure 5.1. Amplitude and phase of Z plotted for the FBARs with different frame configurations

Table 5.1. Comparison of the Q factors and k_{eff}^2 calculated for various frame configurations of the FBAR

FBAR frame configuration	Q_a	Q_r
No frame (basic FBAR)	1607	2523
Single frame for single–mode reflection	1813	2392
Single frame for dual–mode reflection	2305	2491
Dual frame for dual–mode reflection	2605	2590

The advance of dual–mode reflection compared to the single–mode reflection recommended in the literature is demonstrated via the enhancement of the Q_a factors calculated for both the FBARs with a single frame. Of all the simulated FBARs, the one with a dual frame exhibits the highest Q_a. This value increases by approximately 1000 compared to Q_a of the basic FBAR. In Z plots (either amplitude or phase), it provides the sharpest edges at f_a. In addition, the spurious modes in form of the ripples located at the frequencies near and above f_a are well suppressed, providing a smoother electrical characteristic at these

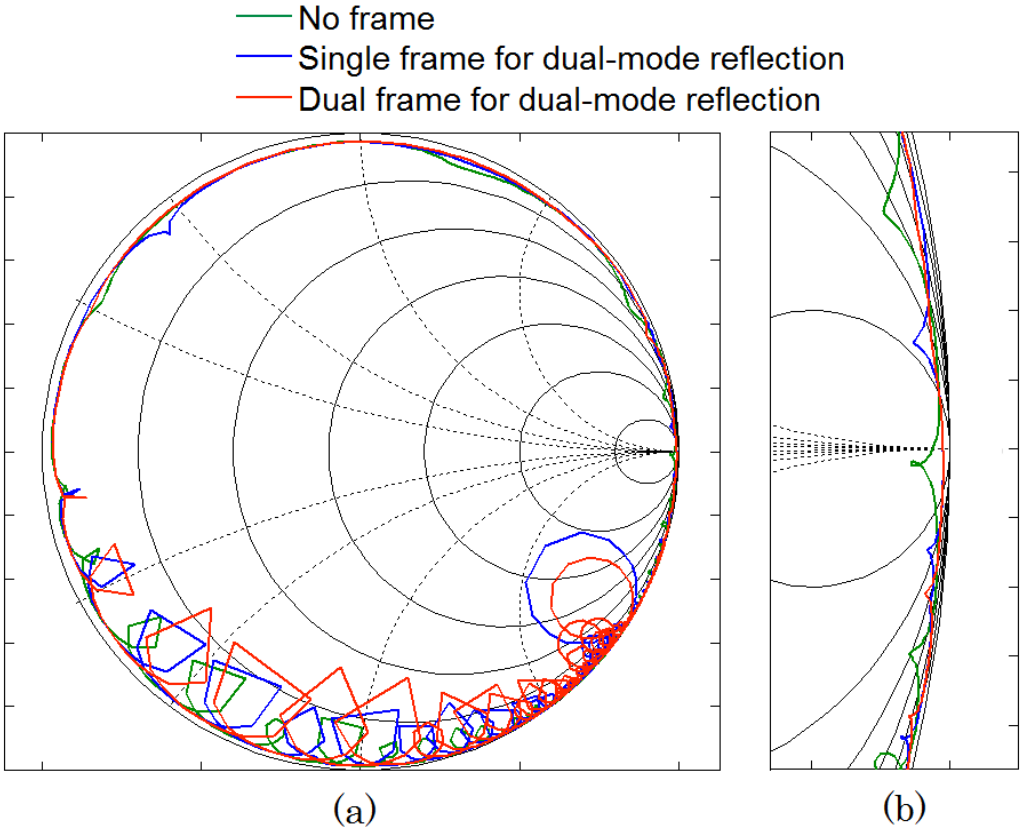

Figure 5.2. Q circles of the FBARs plotted for various frame configurations (a) with close–up vision at the region near the point presenting anti–resonance (b)

frequencies. This can be clearly observed in Figure 5.2 (b) where the red Q circle expands the most without spurious modes near anti–resonance. It should be noted that the sharpness of the edges seen in the phase plot can be translated into the skirt steepness of the filter response. This is to prove the positive influence of the designed frame on the FBAR filter performance.

By referring to (2.33), one may have the explanation for the behavior of Q_r values of various frame configurations. Once metal frame is placed onto the periphery of an FBAR, due to the increasing skin depth, the effective electrode resistance (R_s) of the frame region decreases. The reduction of R_s leads to the enhancement of Q_r. This improvement is more pronounced if larger amount of metal is added (study the tables included in Figure 5.6 and 5.7 for more evidence). At resonance frequency, the leaking waves are inhibited to some degree thanks to the Bragg reflector. These consequently reduce the loss caused by lateral leakage (R_0) and the Q_r value of the resonator is further improved. However, at the same time, the more powerful the frame is designed, the stronger the spurious modes right below resonance are. The spurious modes will steal energy from the main mode for their own operation and thus reduce Q_r. The reduction of R_s and leaking energy in the single–frame FBARs are probably not large enough to compensate the loss caused by spurious modes while this situation is opposite in the dual–frame case. That is why in Table 5.1, the Q_r values of the single–frame FBARs slightly decrease whereas this factor of the dual–frame FBAR increases compared to that of the basic FBAR.

5.2 Impact of the Designed Frame on Preventing Lateral Leakage

The displacement profiles of the area near the outside region of these structures are investigated at their resonance (Figure 5.3) and anti–resonance frequencies (Figure 5.4) in order to provide a better visualization for the impact of the designed frames. Figure 5.3 (b) shows larger displacement amplitude at the top electrode termination, represented by the stronger ripples and the more intense colors compared to those in (a). It means more loss of energy or smaller Q_r value. This situation, however, is less noticeable in Figure 5.3 (c) and (d).

It is interesting to study the displacement profile at anti–resonance frequencies since the designed frame supposes to exhibit its power at these frequencies.

1. The first thing one pays attention to is the intensity of the colors in the active region. The total displacement is expected to reach the minimum

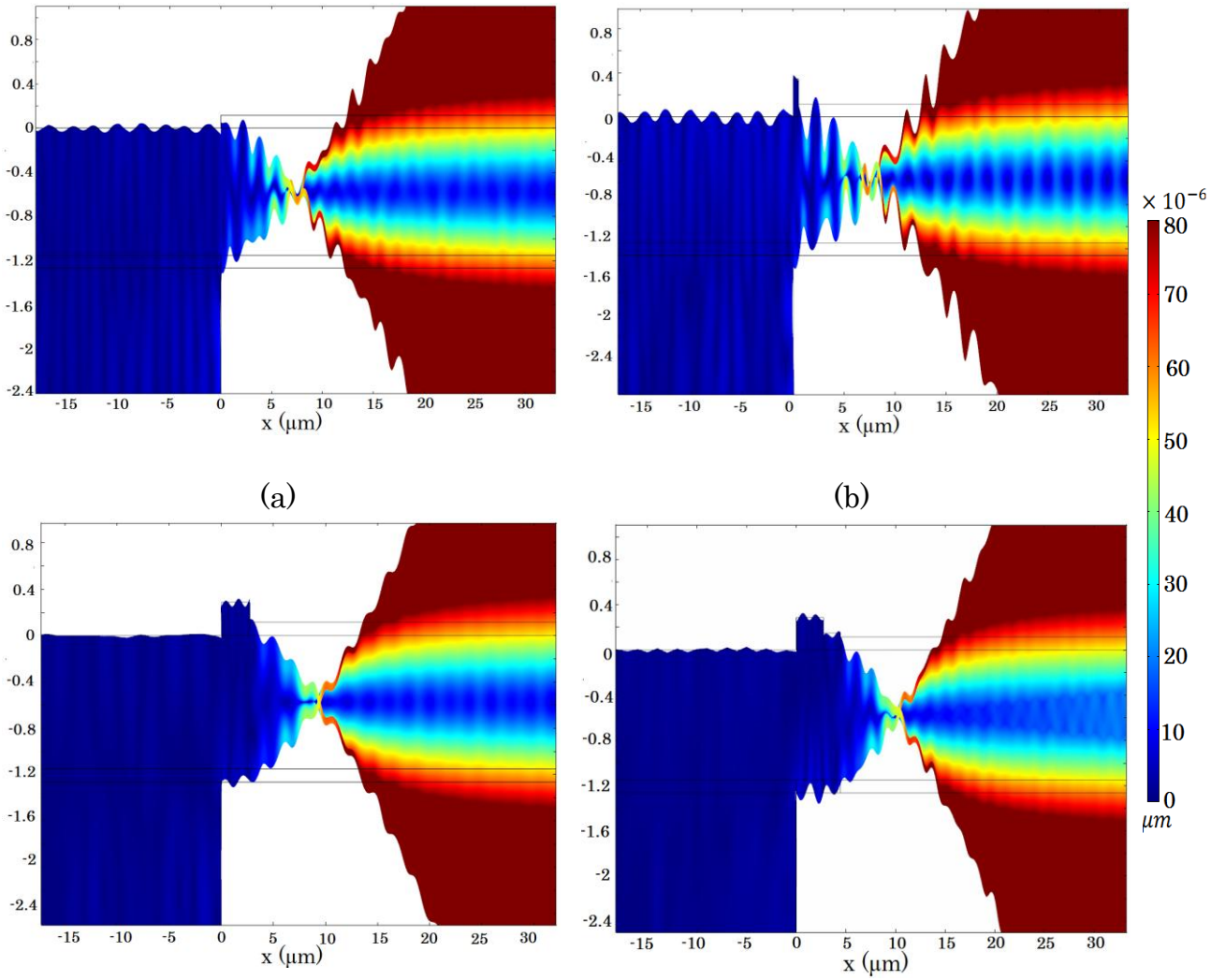

Figure 5.3. Displacement profiles at resonance frequency plotted for the basic FBAR (a), single–frame FBAR for single–mode (b)and dual–mode (c) reflection and dual–frame FBAR (d)

(actually zero in ideal case) at anti–resonance. This speciality is more obvious as we observe sub–plot by sub–plot from (a) to (d) in Figure 5.4.

2. The border region of the FBAR can be considered as a "gate" preventing the acoustic waves from escaping to the outside. While the border region in Figure 5.4 (a) and (b) is remarkably deformed, the one in (c) has less pronounced deformation and this value is even smaller in case of a dual–frame FBAR, meaning that the "gate" is more well–closed in this case.
3. The ripples at outside region represent the travelling of leaking waves. In Figure 5.4 (b), although these waves are weaker than in (a), they are still too evident. It is in contradiction to those presented in (c) and especially in

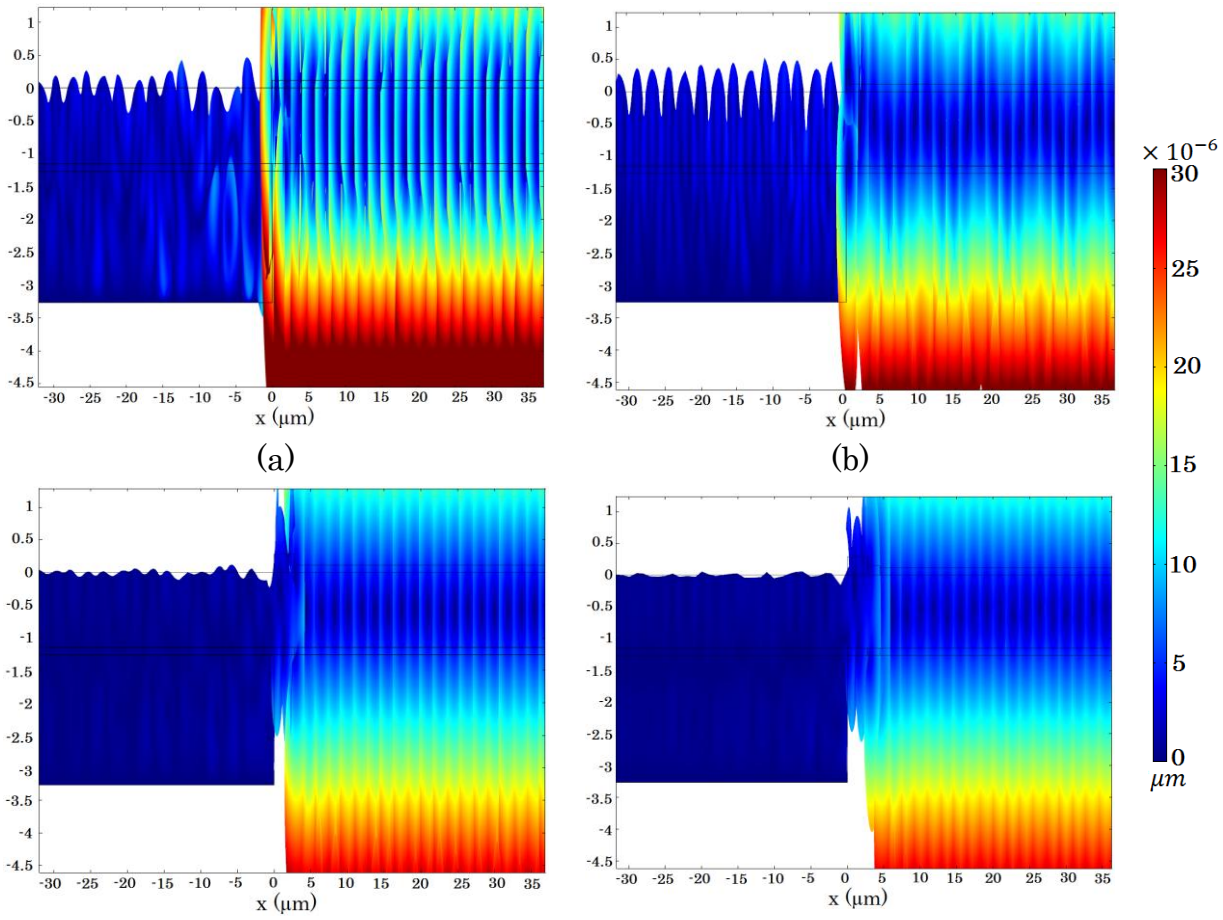

Figure 5.4. Displacement profiles at anti–resonance frequencies plotted for the basic FBAR (a), single–frame FBAR for single–mode (b) and dual–mode (c) reflection and dual–frame FBAR (d)

(d) which is mostly killed by the frame, giving a flatter profile for the outside region.

Since the FBAR with a dual–frame gives the best performance in term of Q factors, it is worth to study further about this structure. The dispersion diagrams are plotted for the electrode region and compared to that of the basic FBAR. Each diagram in Figure 5.5 is also a picture of the energy distribution among symmetric and anti–symmetric modes.

1. Intuitively, the total energy computed at any frequency in Figure 5.5 (b) is higher than in (a). It can be inferred that in case (b), the waves leak to the outside less than in case (a) and energy is better confined in the active region.
2. One might wonder why the colors are blurry around each mode in (b). It is probably due to the coupling of these modes with the main mode.

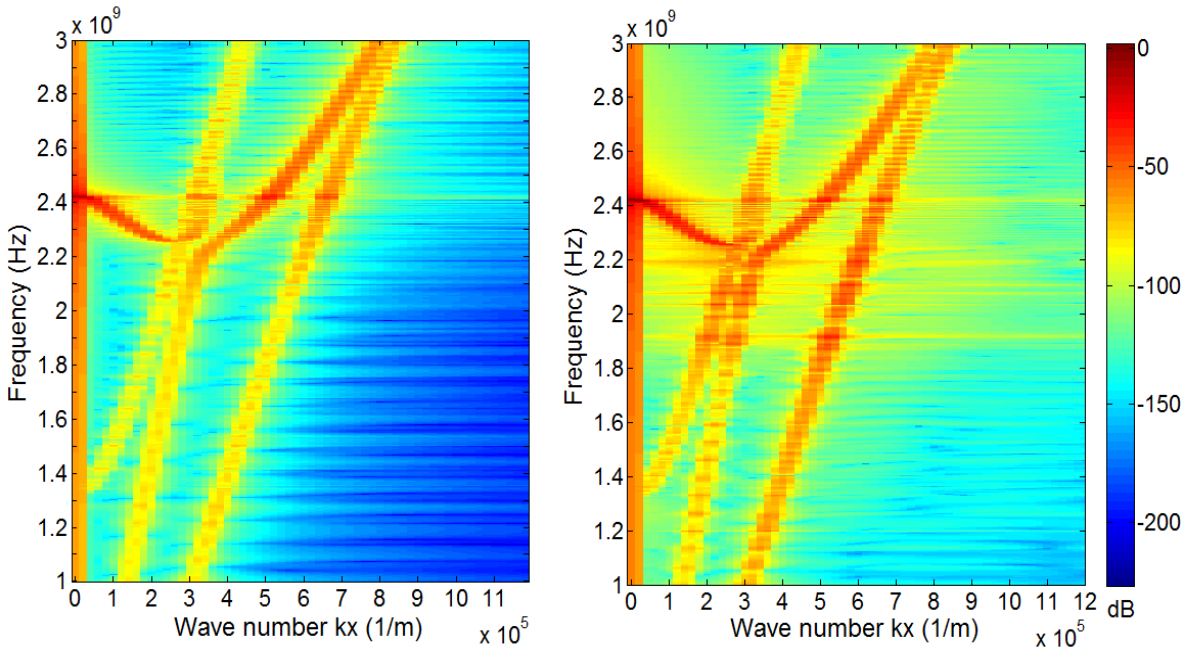

Figure 5.5. Dispersion diagram of the basic (a) and dual–frame FBAR (b) plotted for their metalized regions.

As the lateral waves are trapped in the metalized region, this interaction might be stronger. This causes satellite resonances to occur at some frequencies below the main resonance providing that the interaction is strong enough. From Figure 5.5 (b), it can be predicted that there will be some remarkable ones appearing at 1.92 GHz, 2.03 GHz, 2.07 GHz, 2.11 GHz and 2.20 GHz. This prediction is made based on the observation of the colorful horizontal lines that come across the graph. The intensity of the colors also shows that the most noticeable spurious modes might occur at 1.92 GHz and 2.20 GHz. This anticipation will be made clear via the electrical characteristic in section 5.4.

5.3 Estimation of Tolerances for the Dual–frame Design

It is necessary to check the design tolerance for each individual frame of the dual–frame FBAR. The width of one frame is fixed while that of the other frame is varied by 100 nm for each step. The Q factors are extracted and represented both numerically and graphically in Figure 5.6 and 5.7. Based on this, a tolerable window for each designed frame width is defined. Within that window, the high Q value is assured. In each figure, considering the intersections between the Q_a line and Q_r line, the window length can be defined. The window is approximately 600 nm for the inner frame and 250 nm for the outer one. It can

be concluded that the outer frame was better designed than the inner one. There might be several reasons for this difference

1. The uncertainty from dispersion diagram reading, which can be up to $\Delta = 0.1 \times 10^5$ per meter for each value of k_x, resulting in the deviation of k_x from the correct value.
2. The rounding procedure when calculating the integers m_2 and m_4.
3. Frequency reading error while extracting Q value from COMSOL.

The first one can be overcome by setting a finer mesh for the region where one wants to plot the dispersion diagram. However, it increases the amount of calculation and evidently, simulation time. The second error can be avoided by choosing an appropriate frame height to change k_x of S_0 and S_1 modes in a way that m_2 and m_4 are as near an integer as possible. This is a very difficult task which takes painstaking effort to finish. For example, in a different design for the dual–frame, the author chose an outer frame height of 3.5 times ht, the obtained Q_a is no better than the one of 2.5 times ht due to the larger error (Appendix B.2). The third error is, unfortunately, unavoidable.

It cannot be denied that the obtained Q_a values are not exactly the peak value of the Q curves plotted for the tolerance check. The solutions for the design errors, unfortunately, are laborious and time consuming. Therefore, it is strongly recommended that one should run the tolerance check for the designed frame. By this way, one can find the local maximum Q values and the corresponding widths of the frames within several simulation times. This procedure also has another

Width of the inner frame (nm)	Q_a	Q_r
1300	2241	2550
1400	2629	2547
1500	2848	2558
1600	2903	2565
1700	2877	2573
1800	2825	2574
1900	2727	2582
2000	2605	2590
2100	2465	2585
2200	2188	2585
2300	2354	2604

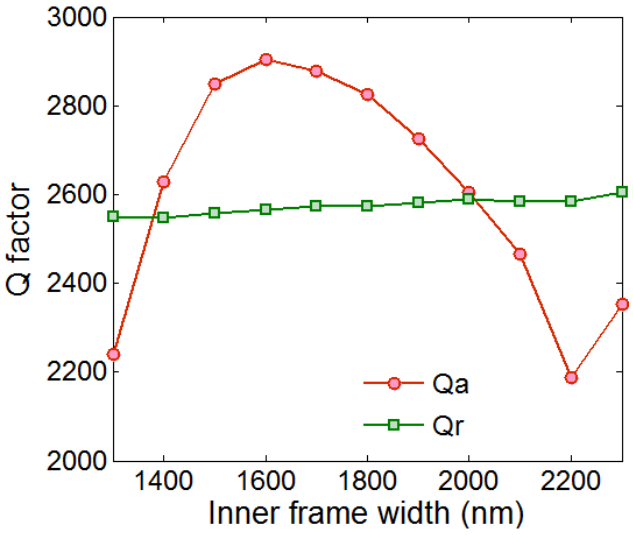

Figure 5.6. Tolerance check for the inner frame, the outer–frame width is fixed

Width of the outer frame (nm)	Q_a	Q_r
2450	2156	2553
2550	2772	2577
2650	2879	2588
2750	2605	2590
2850	2392	2592
2950	2161	2591
3050	2173	2602

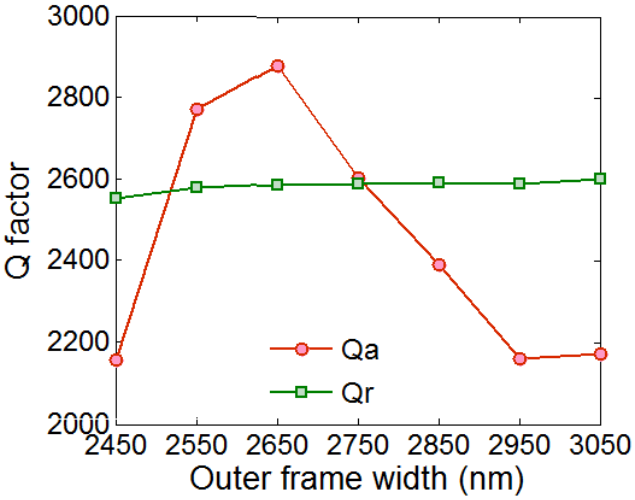

Figure 5.7. Tolerance check for the outer frame, the inner–frame width is fixed

meaning. It indicates the tolerable deviation of the frame width so that the corresponding Q still falls within the "high–Q window". This is an important consideration for the experimental work when one wants to fabricate the frames.

5.4 Side Effects of Lamb Waves Confinement

One of the side effects of the additional frames is the down shifting of anti–resonance frequencies. Since the resonance frequency remains unchanged, this shifting causes the variation in the effective coupling factor as shown in Table 5.2. This shifting effect can be explained using (2.27) and (2.31). The additional frame has increased the effective area due to fringing field thus increases C_0 value and lowers f_a. In the case of a dual frame, the contribution of the fringing field is even larger, therefore f_a drops even more than in the case of a single frame. The applying of a dual frame although help enhance Q_a, it also reduces k_{eff}^2. In other words, k_{eff}^2 was sacrificed in exchange for higher Q factors. Here accounts for the benefit of the layer thickness ratio optimization and material selection to obtain a high k_{eff}^2 from the beginning.

Table 5.2. Frequency pairs and effective coupling factors of the FBARs with different frame configurations

FBAR frame configuration	f_r(GHz)	f_a(GHz)	k_{eff}^2(%)
No frame (Basic FBAR)	2.4225	2.4905	6.55
Single frame for single – mode reflection	2.4225	2.4915	6.64
Single frame for dual – mode reflection	2.4225	2.4890	6.42
Dual frame for dual – mode reflection	2.4225	2.4875	6.28

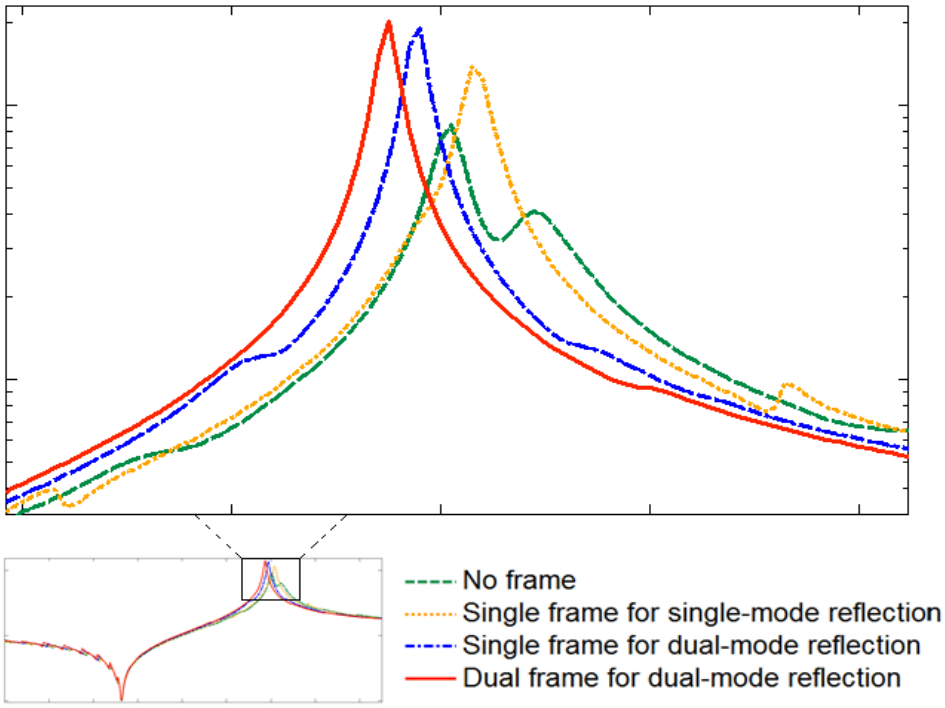

Figure 5.8. The shifting of anti–resonance frequency due to the frames

The confinement of Lamb waves makes the existing spurious resonances right below the resonance frequency more pronounced as well as produces additional unwanted ones due to standing waves. These effects are distinctively clarified in both Figure 5.2 and 5.9.

In general, the spurious modes are the strongest in the case of a dual–frame. This is reasonable because Lamb modes are well trapped in the resonator thus facilitate the lateral standing waves phenomenon. The more leaking waves that was prevented, the more powerful the confinement of the waves and the stronger they resonate and from standing waves. The spurious modes are hence more pronounced. At some certain frequencies, new spurious modes are introduced in the system. The justifications for the "newborn" spurious resonances probably are: a) some of the waves confined in the active region are now strong enough to form new standing waves; b) they are caused by the lateral standing waves that are trapped inside the frame regions; c) they arise from the thickness modes in those regions. The two first reasons are easy to understand while the third one may need to be explained more. In case of the dual frame, due to the differences between two steps, there will be two different frame regions. In total, there are three regions that are metalized – active region, inner frame region, outer frame region. These regions can be considered as three different FBARs that simultaneously operate. The FBAR corresponding to the active region is responsible for the main resonance. The frame regions can be

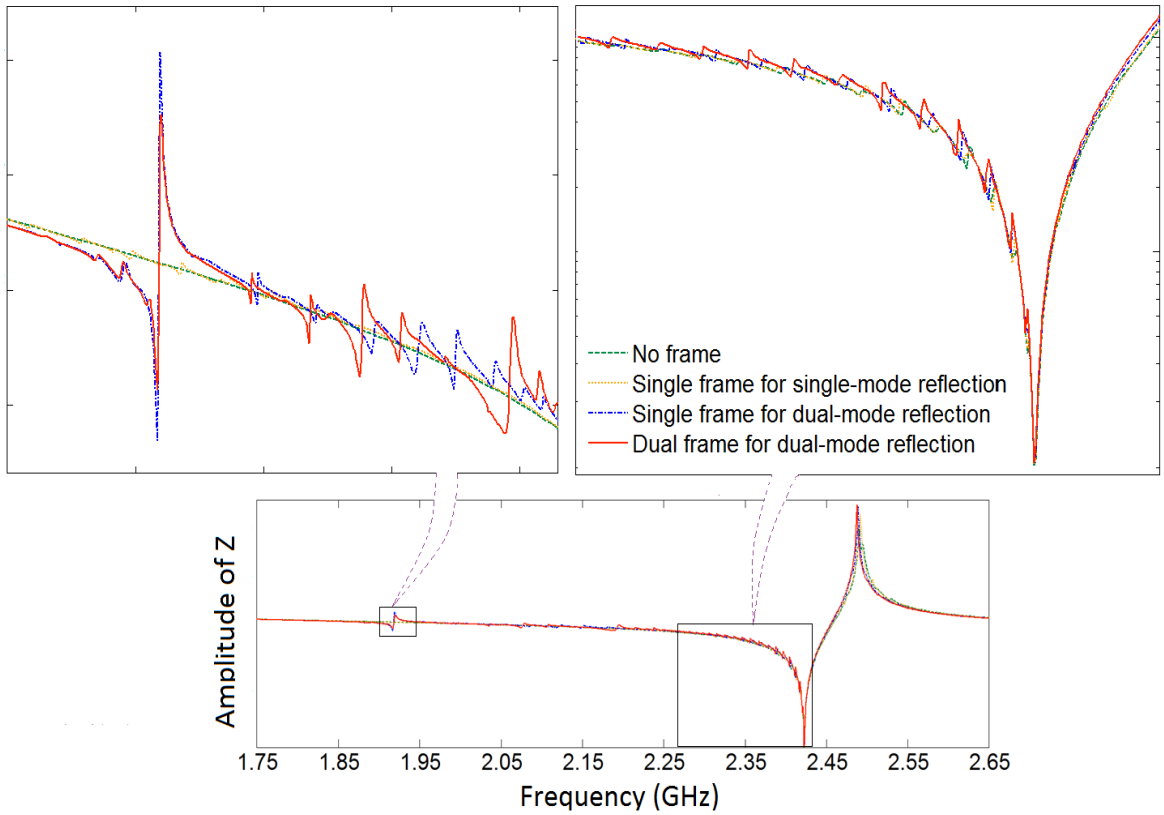

Figure 5.9. The effects of lateral waves confinement on the electrical behavior

understood as independent minor FBARs. The BVD circuits modeled for these minor FBARs are in parallel with the one modeled for the active region, shown in Figure 5.10. The resonance frequencies of these minor FBARs are lower than those of the main resonance because the layer stacks in the frame regions are thicker. These minor resonances suppose to be the new spurious modes. By referring to Figure 4.6 and 4.7 (a) and recalling that the FBAR resonance frequency coincides with the cut–off frequency of S_1 mode, it can be predicted that the minor resonances are at around 1.97 GHz and 2.27 GHz.

Precisely determined from the Z curve, the new spurious modes are pronounced at 1.92 GHz, 2.03 GHz, 2.07 GHz, 2.12 GHz, 2.16 GHz and 2.20 GHz. Most of them agree with the prediction which was made based on the dispersion diagram in sub–section 5.2. The strongest ones at 1.92 GHz and 2.20 GHz are probably the spurious resonances caused by thickness modes in the frame regions. However, they slightly deviate from the predicted ones, which occur at 1.97 GHz and 2.27 GHz. The reason is maybe due to the mechanical constraint at two edges of each frame step. It should be noted that the newborn resonances occur further below the main mode, so they are out–of–band and have minor effects on the filter response shape if one refers to Figure 2.9 (b).

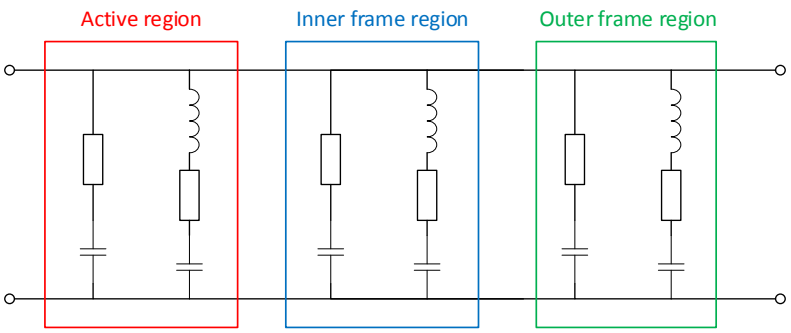

Figure 5.10. BVD model for the FBAR with a dual frame

The stronger spurious modes located right below series resonance, however, are a different story. In a ladder–type filter comprising series and shunt FBAR resonators as shown in Figure 2.9, these modes are going to worsen the unwanted ripples within the left shoulder of the passband. This may lead to the degradation of the filter insertion loss.

The generation of new as well as stronger spurious modes are also the reason for the decreasing of k_{eff}^2. It can be simply understood that since part of the energy supposing to be of the main resonance is now stolen by these modes, the k_{eff}^2 factor which represents for the effectiveness of energy coupling degrades as a result.

5.5 The Repeated Configuration of the Dual Frame

The results extracted for the repeated dual–frame FBAR described in subsection 4.4.3 are given in Table 5.3. As opposed to the expectation of a higher Q_a factor, this structure give a lower Q_a than that of an FBAR with only one dual frame. The degradation of Q_a can be explained by referring to Figure 5.11. The figure shows the new spurious modes introduced to the system as the frames are added. There are two "eye catching" spurious modes in the curve of repeated dual–frame. It is no accident that these two modes coincide with the strongest ones in the dual–frame FBAR case. For the repeated dual frame structure, the numbers of the minor FBARs increase. The two minor FBARs corresponding to two inner frames resonate at the same frequency. It is likewise for the ones that correspond to the outer frames. The BVD model for this structure is depicted in Figure 5.12. Evidently, the amplitude of each additional spurious mode is the contribution of two related FBARs. They are thus much stronger than the ones caused by the dual frame and give rise to the energy loss. It means that R_0 in (2.33) increases, resulting in the decrease of Q_a. Other results such as the increase of Q_r, the down shifting of f_a and the reduction of k_{eff}^2 agree with the explanations that were already given for the dual–frame case. From this result,

for the lateral ABR, the design of one acoustic mirror pair is sufficient for the demand of a high–Q resonator.

Table 5.3. Results of the repeated dual–frame FBAR

Q_a	Q_r	f_r (GHz)	f_a (GHz)	k_{eff}^2
2210	2938	2.4225	2.4815	5.73%

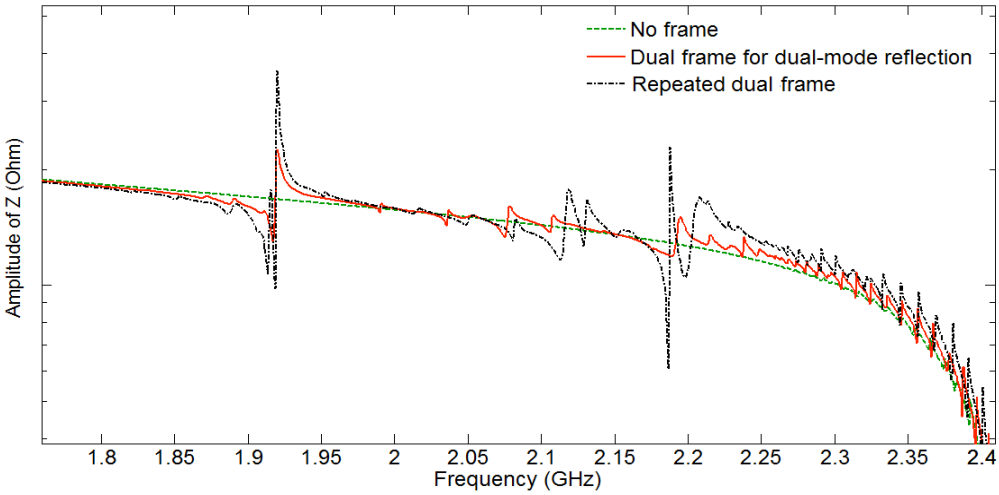

Figure 5.11. The new spurious modes in various FBAR frame configurations

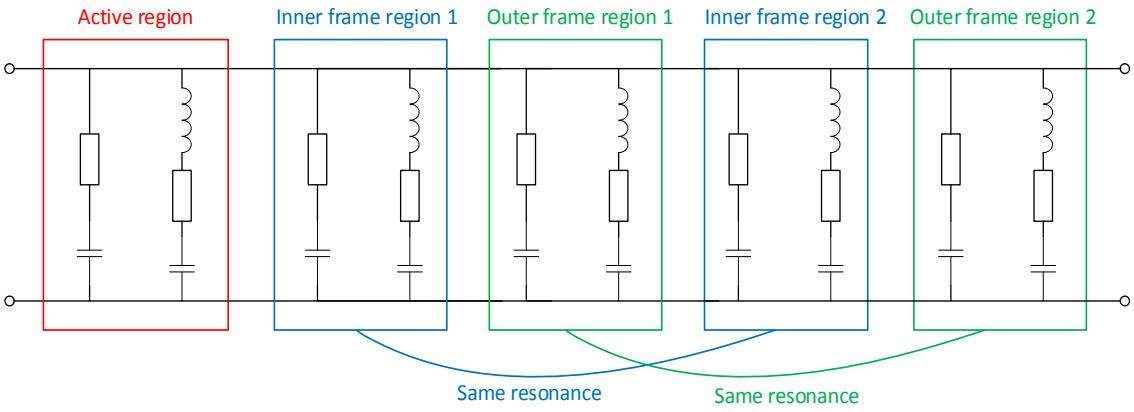

Figure 5.12. Equivalent circuit of the FBAR with two pairs of acoustic mirror

5.5.1 The Impact of Dielectric Loss on Q_a factor

For the deposition of AlN layer, the material quality, particularly the dielectric loss factor may vary upon different process techniques. The loss factor chosen for the previous simulations is 0.002, falling within a reported range of 0.0005 – 0.01 [46]. This value is higher for poor quality AlN layer. Table 5.4 shows the impact of this loss on the Q_a factor, by which proves the importance of fabricating a low loss piezo–layer. From the table, it can be inferred that

Table 5.4. Q_a factors calculated for various values of dielectric loss

Dielectric loss factor (tanδ)	Q_a of the basic FBAR	Q_a of the dual–frame FBAR
0.002	1607	2605
0.004	1462	2059
0.006	1328	1703
0.008	1221	1469
0.01	1136	1290

1. Higher dielectric loss means lower Q_a value, no matter that the resonator is optimized or not.
2. As the loss factor is higher, the impact of the designed frame on Q_a tends to be weaker. For example, for tanδ = 0.002, Q_a of a dual–frame FBAR increases 62.1% compared to that of a basic FBAR while Q_a increases only 13.6% for tanδ = 0.01. It seems that the internal loss in the second case is too high so the amount of lateral leakage is not noticeable anymore. The power of the frame is hence not as distinctive as in the first case.
3. A high quality AlN layer is crucial if one aims to produce a high Q resonator.

5.6 Chapter Summary

This chapter declares the obtained results for the optimization. It is shown that the frame has helped enhance the resonator quality factors, exclusively at the anti–resonance frequency. The dual–step frame designed for dual–mode reflection provides even better Q factors thanks to the superior wave trapping. The spurious modes near anti–resonance are well suppressed. However, the confinement of waves has brought some unwanted side effects, involving the degradation of effective coupling factor and the unwanted stronger spurious modes below series resonance frequency.

CHAPTER 6. Conclusions and Future Works

Basic FBAR resonators, although promises higher Q factors than its brother SMR technology as it does not experience the acoustic leakage in thickness direction, still demands an enhancement of Q for filter applications, especially for those that operate at the frequencies beyond 2 GHz. This thesis has studied the structure of an FBAR as well as its operating principle based on piezoelectric phenomenon. It has also analyzed the possible energy loss mechanisms in the resonator. If these loss mechanisms are somehow restrained, a high Q state–of–the–art FBAR can be assured. One mechanism that draws the attention of this work is the lateral wave leakage. For such a resonator that is finite in all dimensions like the FBAR, the excitation and propagation of Lamb waves in lateral direction is inevitable. Problem arises when these waves leak to the outside region causing loss of energy and degradation of Q value. In this thesis, this problem is solved by the application of a frame structure which can confine these waves and force them to reflect back into the active region. By reducing the leaking waves, the high Q value can be achieved. In fact, the frame method was already introduced in other research papers. Although the final purpose is also to improve the resonator quality factor, the frame they mentioned was applied to eliminate a different loss mechanism – the spurious modes. The effects of the frames, which are designed by these two different techniques, on the whole system are therefore not quite similar.

Chapter 3 of this thesis explains the method to design such frame. The advance of the method can be summarized into two points

1. It takes advantage of the variation in acoustic impedances between electrode regions so the Bragg's law can be fully applied for the frame in lateral direction, so called the lateral acoustic Bragg reflector.
2. The frame is able to reflect two modes at a time thus more effectively prevent energy from leaking compared to the traditional Bragg reflector.

The theory provided in Chapter 3 is verified in Chapter 4 which describes how a model of the optimized FBAR is built and simulated in COMSOL software. The procedure includes selecting the appropriate materials, choosing the layer thickness ratio which provides the highest coupling factor, plotting the dispersion diagrams for various thicknesses of top electrode, extracting data from the dispersion curves and calculating the frame width before placing it onto the periphery of the top electrode. Two types of frame structure are implemented

– a single frame and a dual frame. From the simulation results, the Q factors are calculated using 3dB bandwidth method for each case. The obtained results are compared to those of a basic FBAR without any modification at the border region and of an FBAR with a single frame that can only reflect one wave mode. Among all, the FBAR with dual–frame gives the highest Q value, proving the robustness of the introduced solution. Further than that, the ripples in the vicinity of anti–resonance frequency are smoothened, meaning that the spurious modes at these frequencies have been suppressed.

Although the achieved results are good as expected, the work does have its own limitations.

1. The design requires more masks, i.e. more complicated manufacturing process and higher cost.
2. The Q_a factor is not the highest possible value due to the uncertainties and errors coming from the restriction in simulation time and the approximation in frame width computations.
3. Unwanted side effects of the method, including the decrease of coupling factor and the more pronounced spurious modes below the resonance frequency.

The spurious modes are the most considerable problem when the designed FBAR is utilized in a filter. They can cause strong ripples in the passband and worsen the shape of the filter response. The solution to this problem, fortunately, has been published in literature. It is called the "apodization" method and can be combined with the frame method proposed in the thesis. In this method, the geometry of the top electrode is modified so that no parallel edges can co–exist and no vertices has an angle near 90^o. The top electrode might be in elliptical, pentagon, hexagon or irregular convex polygon shape (as in Figure 6.1). These shapes are recommended in order to avoid the same lateral resonance path length in the active region thus smear out the lateral standing waves and minimize the amplitude of spurious resonances. To evaluate the effect of this method in COMSOL, a 3D model of the FBAR is required.

If one looks into the dispersion diagram in Figure 3.10 (a), one may observe that the A_0 mode is also a strong mode that carries a large amount of energy. For the frequencies above f_s, it is even stronger than S_1 mode. By intuition, the dual–mode reflection theory might be applied for either A_0 and S_0 modes or A_0 and S_1 modes instead of the two modes considered in this thesis. If this prediction is correct, the Q factors for the two first cases might be similarly enhanced or even better.

The simulated FBAR did not take into account the effect of temperature. In fact, AlN and W have negative temperature coefficient for the stiffness [23]. In other words, their stiffness constants decrease as the temperature increases. In that case, the addition of other layers for temperature compensation is necessary. Those layers are silicon dioxide thin films deposited under the bottom and over the top electrode as in Figure 6.2. This compensating will ensure the stability for those devices working in high temperature environment.

All the mentioned considerations aim for an FBAR with the best performance. However, it is still a simulated model. If one wants to verify how the resonator works in reality, the first thing to do is to fabricate it. The manufacturing process may include metal deposition, AlN deposition – which is a very sophisticated work since a high quality film is required, patterning the frame, etc… A fabrication process for FBAR resonators may be found in [6]. Once finished, the electrical behavior of the resonator on wafer level should be measured and characterized before being used to create a filter that fulfills the demand of selectivity, bandwidth as well as insertion loss in modern applications.

Since the dual frame structure is critical for the FBAR design, the process for fabricating it should be carefully considered. In fact, the fabrication of these frames as well as the deposition of a high quality AlN layer, are the most challenging. Single crystal tungsten metal is isotropic. For wet–etch bulk micromachining of Tungsten using alkaline Hexacyanoferrate (III) etchant, with 0.9 mol/l of KOH, 0.15 mol/l of $K_3FE(CN)_6$ and 1% of Tergitol etchant at 25^oC, the etch rate is 20 nm/s at 100 mA/cm^2 and 80 nm/s at 460 mA/cm^2 [49]. The material will be etched in all directions with a very high rate. Using this method to create the frames is not feasible. For dry etching in pulse SF_6 plasma, the etch rate is around 3 nm/s at 0^oC, 5 nm/s at 30^oC or 13 nm/s at 80^oC [49]. The process for dry etching is thus easier to control than for wet etching. However, controlling the thickness of each layer is also a big challenge. It seems that subtracting technique like etching is not appropriate in this situation. Therefore, additive technique such as metal lift–off should be used to solve the thickness control problem. The width of the etched frame is required to deviate less than several hundred nanometers from the peak value (maximum Q) so that the Q factors are still in the "safe" window. It means the lithography technique used to transfer the pattern from the mask to the substrate must have high resolution. In theory, by using photolithography method with glass mask and vacuum contact mode, one can achieve the resolution in submicron range [50]. However, this resolution is not assured in reality and the misalignment (may be 1 to few

microns) is also a big challenge. To be sure that the frame is fabricated with the tolerable width, the electron beam lithography technique is recommended. This method provides a better resolution (down to 5 nm) and smaller misalignment (down to 0.46 nm) [51] in exchange for a higher manufacturing cost.

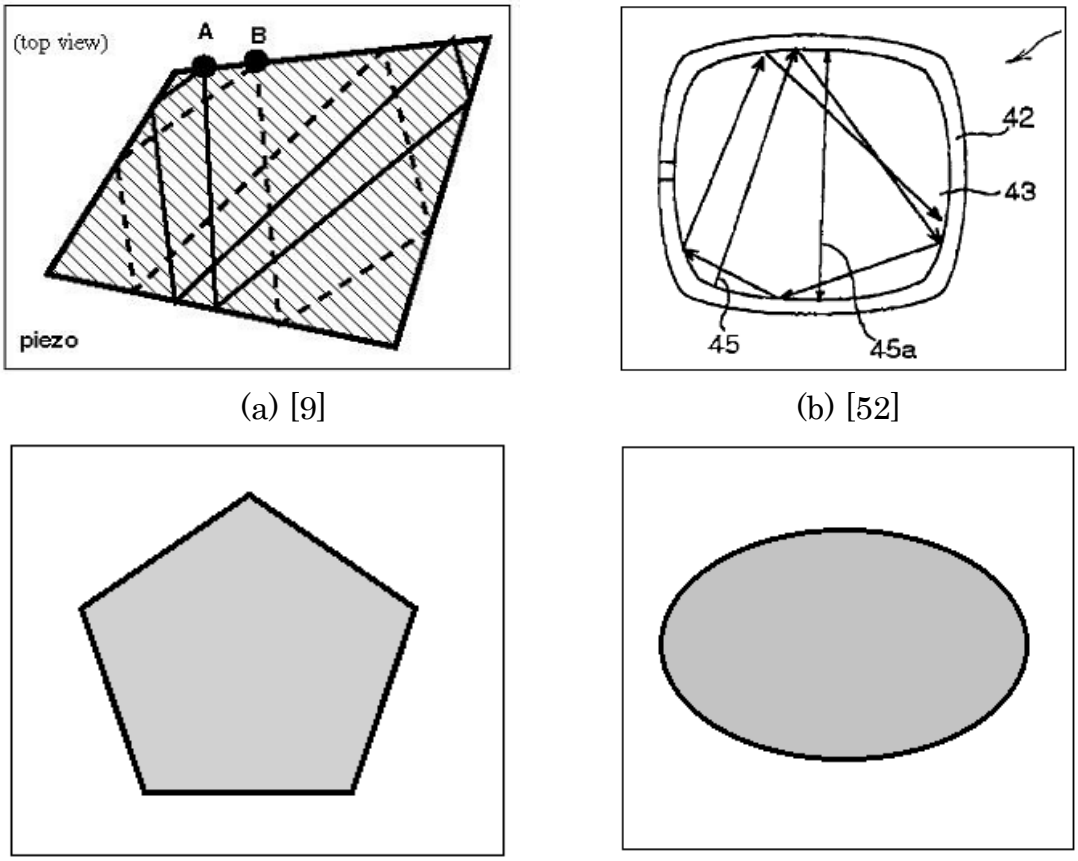

(a) [9] (b) [52]

(c) (d)

Figure 6.1. Apodized top electrode shapes

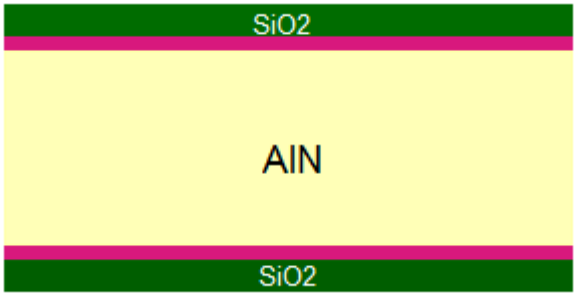

Figure 6.2. Layer stack for temperature conmpensation

The FBAR in this thesis supposes to operate in S–band frequency in which the requirement for a high coupling factor is not so strict. With the use of frames, one may even trade the coupling factor for better Q values. However, for those

higher demanding applications, e.g. the devices working in the C–band[10], this trading is feasible provided that they have a more superior coupling factor. The reason is the applications for this band require higher k_{eff}^2. To satisfy this, another promising method named "boundary frame" has been proposed in [19, 22]. An additional layer of silicon dioxide is deposited on the piezo–layer (Figure 6.3) in advance to add a frame. If the FBAR designed based on this method can provide good Q factors, it is worth to be investigated.

Figure 6.3. The boundary frame method

[10] Operating frequency range falls within 4 – 8 GHz, according to IEEE standards.

Appendix A

MATLAB codes for extracting the dispersion diagram

```
%% Declaration
a=importdata('Filename.csv',' ');
X=a(:,1);
p=1; Wa=500; Lactive=50e-6;
%% Extracting data for the active region
for c=1:length(X)
    if (X(c)>=0)
      X(p)=X(c);
      a(p,:)=a(c,:);
      p=p+1;
    end
end
S= size(a,2);
u= zeros(Wa+1,S);
%% Extracting data for surface only
 q=1;
 for row= 1:size(a,1)
     if a(row,2)== 0
         X(q)= X(row);
         u(q,:)= a(row,:);
         q=q+1;
     end
 end
u= u(:,3:end);
uz= u';
%% Hann windowing and Spatial FFT for each row to change into the
%  wave number domain
L= size(uz,2);
uz1= zeros(size(uz));
U= zeros(size(uz));
W= hanning(L); % generate a M point symmetric Hanning window
for m= 1:size(uz,1) % scan the row of matrix uz
    uz1(m,:)= W'.*uz(m,:); % applying Hanning window
    U(m,:)= fft(uz1(m,:),L);% Fourier transform for each row
end
U1= 20*log10(abs(U)); % amplitude to decibel conversion
n= 0:L-1;
% Calculate the number of unique points
UniquePts = ceil((L+1)/2);
% FFT is symmetric, throw away second half
n = n(1:UniquePts);
k= n/Lactive;
U2= U1(1:end,1:UniquePts);
% plot
f= 1e9:5e5:3e9;
figure(1)
imagesc(k,f,U2);
set(gca,'YDir','normal')% flip the y axis
```

Appendix B

1. **Frame widths calculated for various corresponding frame heights for optimization at anti–resonance frequency**

Frame height		$1.3 * ht$	$1.5 * ht$	$1.7 * ht$	$2 * ht$	$2.5 * ht$	$3 * ht$	$3.5 * ht$
$k_x(S_1)$	(1/μm)	0.39	0.40	0.41	0.43	0.45	0.47	0.48
Quarter wavelength of S_1	(nm)	641	625	610	581	556	532	521
$k_x(S_0)$	(1/μm)	0.60	0.62	0.63	0.63	0.64	0.64	0.64
Quarter wavelength of S_0	(nm)	417	403	397	397	391	391	391
$K = \frac{k_x(S_0)}{k_x(S_1)}$		1.538	1.550	1.537	1.465	1.422	1.362	1.333
m_1		1	1	1	2	2	2	2
Calculated m_2		1.808	1.829	1.805	3.163	3.056	2.904	2.833
Rounded m_2		2	2	2	3	3	3	3
Frame width for m_1	(nm)	1923	1875	1830	2905	2780	2660	2605
Frame width for m_2	(nm)	2085	2015	1985	2779	2737	2737	2737
Deviation between calculated frame widths	(nm)	162	140	155	126	43	70	132

2. Dual–frame design with outer frame height of 3.5*ht and FBAR performance

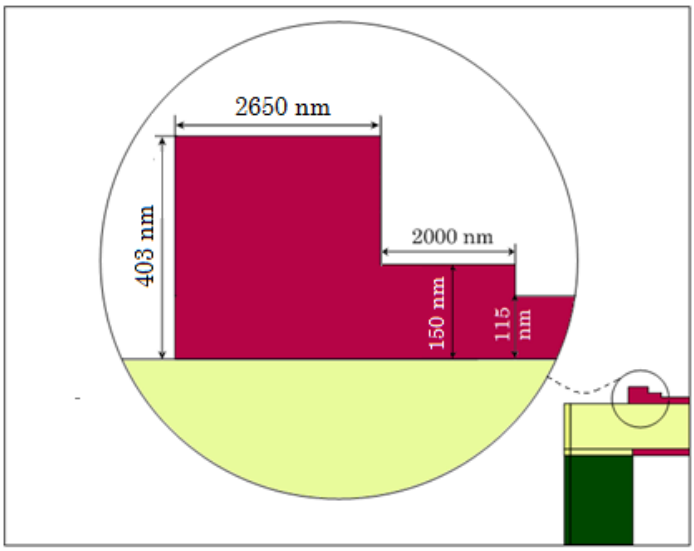

$f_a = 2.4870\ GHz$
$f_r = 2.4225\ GHz$
$Q_a = 2400$
$Q_r = 2549$
$k_{eff}^2 = 6.23\%$

References

1. Lakin, K.M. and J.S. Wang, *Acoustic bulk wave composite resonators.* Applied Physics Letters, 1981. 38(3): p. 125-127.
2. Dubois, M.-A., *Thin film bulk acoustic wave resonators: a technology overview.* 2003, MEMSWAVE 03: Toulouse, France.
3. Aigner, R., *SAW, BAW and The Future of Wireless.* http://www.edn.com, 2013.
4. Ruby, R. *11E-2 Review and Comparison of Bulk Acoustic Wave FBAR, SMR Technology*. in *Ultrasonics Symposium, 2007. IEEE*. 2007.
5. Aigner, R. *SAW and BAW technologies for RF filter applications: A review of the relative strengths and weaknesses*. in *Ultrasonics Symposium, 2008. IUS 2008. IEEE*. 2008.
6. Campanella, H., *Acoustic wave and electromechanical resonators : concept to key applications*. Integrated microsystems series. 2010, Norwood, MA.: Artech House. xv, 345 p.
7. Ruby, R. and P. Merchant. *Micromachined thin film bulk acoustic resonators*. in *Frequency Control Symposium, 1994. 48th., Proceedings of the 1994 IEEE International*. 1994.
8. Thalhammer, R. and R. Aigner. *Energy loss mechanisms in SMR-type BAW devices*. in *Microwave Symposium Digest, 2005 IEEE MTT-S International*. 2005.
9. Link, A., et al. *Appropriate Methods to Suppress Spurious FBAR Modes in Volume Production*. in *Microwave Symposium Digest, 2006. IEEE MTT-S International*. 2006.
10. Ruby, R., et al. *The effect of perimeter geometry on FBAR resonator electrical performance*. in *Microwave Symposium Digest, 2005 IEEE MTT-S International*. 2005.
11. Larson, J.D., R.C. Ruby, and P. Bradley, *Bulk acoustic wave resonator with improved lateral mode suppression*. 2001, Google Patents.
12. Rosen, D., J. Bjurstrom, and I. Katardjiev, *Suppression of spurious lateral modes in thickness-excited FBAR resonators.* Ultrasonics, Ferroelectrics and Frequency Control, IEEE Transactions on, 2005. 52(7): p. 1189-1192.
13. Hosoo, P., et al. *Advanced lateral structures of BAW resonator for spurious mode suppression*. in *Microwave Conference (EuMC), 2012 42nd European*. 2012.
14. Kaitila, J., et al. *Spurious resonance free bulk acoustic wave resonators*. in *Ultrasonics, 2003 IEEE Symposium on*. 2003.
15. Feng, H., et al., *Thin film bulk acoustic resonator with a mass loaded perimeter*. 2007, Google Patents.
16. Thalhammer, R., et al. *Prediction of BAW resonator performance using experimental and numerical methods*. in *Ultrasonics Symposium, 2004 IEEE*. 2004.
17. Fattinger, G.G., et al. *Optimization of acoustic dispersion for high performance thin film BAW resonators*. in *Ultrasonics Symposium, 2005 IEEE*. 2005.
18. Thalhammer, R., et al. *4E-3 Spurious Mode Suppression in BAW Resonators*. in *Ultrasonics Symposium, 2006. IEEE*. 2006.
19. Pensala, T. and M. Ylilammi, *Spurious Resonance Suppression in Gigahertz-Range ZnO Thin-Film Bulk Acoustic Wave Resonators by the Boundary Frame Method: Modeling and Experiment.* Ultrasonics, Ferroelectrics and Frequency Control, IEEE Transactions on, 2009. 56(8): p. 1731-1744.

20. Kuwano, M.H.a.H., *Spurious Suppression without Energy Dissipation in Aluminum–Nitride-Based Thin-Film Bulk Acoustic Resonator Using Thin Ring on Electrode Edge* Jpn. J. Appl. Phys., 2012. 51(7S).
21. Hara, M., M. Ueda, and Y. Satoh, *A thin-film bulk acoustic resonator and filter with optimal edge shapes for mass production.* Ultrasonics, 2013. 53(1): p. 90-96.
22. Kumar, P.T., C. C. , *Design of a New Step-like Frame FBAR for Suppression of Spurious Resonances.* Radioengineering, 2013. 22(3): p. 687.
23. Hashimoto, K., *RF Bulk Acoustic Wave Filters for Communications*. 2009: ARTECH HOUSE
24. Jose, S., A.B.M. Jansman, and R.J.E. Hueting. *A design procedure for an acoustic mirror providing dual reflection of longitudinal and shear waves in Solidly Mounted BAW Resonators (SMRs)*. in *Ultrasonics Symposium (IUS), 2009 IEEE International*. 2009.
25. Jose, S., et al., *Optimized reflector stacks for solidly mounted bulk acoustic wave resonators.* Ultrasonics, Ferroelectrics and Frequency Control, IEEE Transactions on, 2010. 57(12): p. 2753-2763.
26. Ruby, R.C., et al. *Thin film bulk wave acoustic resonators (FBAR) for wireless applications*. in *Ultrasonics Symposium, 2001 IEEE*. 2001.
27. Rosenbaum, J.F., *Bulk acoustic wave theory and devices*. The Artech House acoustics library. 1988, Boston: Artech House. xiv, 462 p.
28. Bi, F.Z. and B.P. Barber, *Bulk acoustic wave RF technology.* Ieee Microwave Magazine, 2008. 9(5): p. 65-80.
29. Schott, F.W., *On the Smith Chart (Letters).* Microwave Theory and Techniques, IEEE Transactions on, 1978. 26(4): p. 314-314.
30. Caspers, F., *RF engineering basic concepts: the Smith chart.* CAS-CERN, Geneva, Switzerland, 2012: p. 2.
31. Auld, B.A., *Acoustic fields and waves in solids*. 2nd ed. Vol. II. 1990, Malabar, Fla.: R.E. Krieger.
32. Rose, J.L., *Ultrasonic waves in solid media*. 1999, Cambridge, U.K. ; New York: Cambridge University Press. xvi, 454 p.
33. Ruby, R.C., et al. *Performance degradation effects in FBAR filters and resonators due to lamb wave modes*. in *Ultrasonics Symposium, 2005 IEEE*. 2005.
34. Kokkonen, K., T. Pensala, and M. Kaivola, *Dispersion and mirror transmission characteristics of bulk acoustic wave resonators.* Ultrasonics, Ferroelectrics and Frequency Control, IEEE Transactions on, 2011. 58(1): p. 215-225.
35. Hora, P., Červená, O., *Determination of Lamb Wave dispersion curves by means of Fourier transform.* Applied and Computational Mechanics 2012. 6(1): p. 5-16.
36. Perrin, C.L., *Numerical recipes in Fortran 90: The art of scientific computing, second edition, volume 2.* Journal of the American Chemical Society, 1997. 119(37): p. 8748-8748.
37. Ingle, V.K. and J.G. Proakis, *Digital signal processing using MATLAB V.4*. 1997, Boston, Mass. ; London: PWS Publishing Company.
38. Kaitila, J., *3C-1 Review of Wave Propagation in BAW Thin Film Devices - Progress and Prospects.* Proc IEEE Ultrason Symp, 2007: p. 120-129.
39. D'hondt, M., P. Modak, and I. Moerman, *Distributed Bragg Reflector comprising a GaP layer, and a semiconductor resonant cavity device comprising such a DBR*. 2003, Google Patents.
40. Wentao, W. and D. Weinstein. *Acoustic Bragg reflectors for Q-enhancement of unreleased MEMS resonators*. in *Frequency Control and the European Frequency and Time Forum (FCS), 2011 Joint Conference of the IEEE International*. 2011.

41. www.olympusmicro.com/primer/lightandcolor/mirrorsintro.html.
42. www.ntt-review.jp.
43. Chih-Ming, L., C. Yung-Yu, and A.P. Pisano, *Theoretical investigation of Lamb wave characteristics in AlN/3C–SiC composite membranes.* Applied Physics Letters, 2010. 97(19): p. 193506-193506-3.
44. Pensala, T., *Thin Film Bulk Acoustic Wave Devices*. 2011, School of Science - Aalto University: Finland.
45. Auld, B.A., *Acoustic fields and waves in solids*. 2nd ed. Vol. I. 1990, Malabar, Fla.: R.E. Krieger.
46. Savrun, E., N. Vu, and N. Gilmore. *High thermal conductivity aluminum nitride ceramics for high power microwave windows - An update*. in *Vacuum Electronics Conference, 2004. IVEC 2004. Fifth IEEE International*. 2006.
47. Lakin, K.M., et al. *Improved bulk wave resonator coupling coefficient for wide bandwidth filters*. in *Ultrasonics Symposium, 2001 IEEE*. 2001.
48. Brotz, J., *Damping in CMOS-MEMS Resonator*, in *Electrical and Computer Engineering*. 2004, Carnegie Mellon University: Carnegie Mellon University. p. 78.
49. Köhler, M., *Chosen Recipes*, in *Etching in Microsystem Technology*. 2007, Wiley-VCH Verlag GmbH. p. 179-344.
50. SussMicroTec, *MJB4 Mask Aligner datasheet*.
51. http://www.jwnc.gla.ac.uk/electronbeamlithography.html.
52. Yang, D.Y., Kim H. W., *Film bulk acoustic resonator with improved lateral mode suppression* in *United States Patent*. 2004: US. p. 1.